Technical Report
TR-19-13
April 2019

Stress corrosion testing of copper in near neutral sulfide solutions

Claes Taxén
Jesper Flyg
Hans Bergqvist

SVENSK KÄRNBRÄNSLEHANTERING AB

SWEDISH NUCLEAR FUEL
AND WASTE MANAGEMENT CO

Box 3091, SE-169 03 Solna
Phone +46 8 459 84 00
skb.se

SVENSK KÄRNBRÄNSLEHANTERING

ISSN 1404-0344
SKB TR-19-13
ID 1708667

April 2019
Updated 2019-11

Stress corrosion testing of copper in near neutral sulfide solutions

Claes Taxén, Rise KIMAB AB

Jesper Flyg, Hans Bergqvist
Swerim AB

The original report, dated April 2019, was found to contain an editorial error which have been corrected in this updated version.

Summary

Copper rods were tested for signs of stress corrosion cracking in salt solutions with different sulfide concentrations. The pH of the test solutions were kept near neutral by addition of 10 mM phosphate buffer of pH 7.2. Tests were performed by slow strain rate testing at 90 °C and at 60 °C. The extension rate was 5×10^{-7} s^{-1} until rupture for most tests whereas some were interrupted after a few days of testing. Cross sections of the specimens were investigated with SEM (scanning electron microscopy).

Results showed intergranular corrosion in the shape of cracks at a level of 1 mM sulfide at 60 °C and at 90 °C. Tests under similar conditions with 0.02 mM sulfide did not result in such intergranular corrosion but only an uneven surface.

Stress-strain curves do not reveal any signs of stress corrosion cracking. The time to final rupture and the elongation at rupture are independent of the test conditions used.

Intergranular corrosion in the shape of cracks develops early during the test. Tests interrupted after 2 or 4 days of strain reveal a number of cracks preferentially located towards the ends of the gauge length of the test rod. At final rupture of the test rods, after about 14 days of continuous strain, the cracks are more evenly distributed along the test rod.

Necking and final rupture occurs close to the middle of the gauge length and not at the location where the first cracks appear. The maximum depth of the cracks is estimated to about 20–30 µm. The maximum depth of cracks found after final rupture does not significantly exceed that found after 2 or 4 days.

Results are discussed in terms of mechanisms for intergranular corrosion with a possible spatial separation between anodic and cathodic sites. One role of the strain is suggested to be cracking of a layer of corrosion products that otherwise would be protecting. Another role of stress and strain could be to aggravate intergranular corrosion at sites where gaps in the protective layer coincides with a susceptible grain boundary.

Intergranular corrosion seems to produce dissolved copper sulfide species as primary corrosion products. Formation of the more stable $Cu_2S(s)$ takes place outside the cavities formed, at least initially. The rate of propagation is then limited by the rate of diffusion of dissolved copper sulfide complex species from the front of the cavity to the mouth of the cavity. Eventually, solid Cu_2S forms also inside the cavity. Cu_2S is predicted to form in increasing proportions, inside the cavity, as more surface becomes available for crystal growth and the fraction of the oxidized copper that diffuses out from the cavity decreases. Because of the volume increase when copper metal is corroded to Cu_2S, the cavity will tend to fill up with Cu_2S. Finally, the cavity will be filled with solid corrosion products and unless continued strain creates new aqueous volume in the cavity, propagation will stop.

Contents

1 Introduction

In a previous study copper was tested for signs of stress corrosion cracking (SCC) in 10 mM sulfide solutions at 80 °C with an extension rate of 1×10^{-6} s^{-1} (Taxén et al. 2018). No signs of SCC were detected. Parallel to this work, the Swedish Radiation Safety Authority (SSM) carried out studies of SCC of copper in sulfide solutions at Studsvik (Becker and Öijerholm 2017). For tests at 90 °C, they found features that were interpreted as signs of SCC.

In the present work test conditions were selected to be similar to those used by Becker and Öijerholm. The aim of the work was to replicate parts of the tests by Becker and Öijerholm and to study the influence of various test parameters on the tendency for SCC of copper in sulfide solutions.

2 Experimental

2.1 Material

The copper material was supplied by SKB and cut from lid TX#219. Test rods were cut from the base material by spark cutting followed by turning into shape. The test rods were fully annealed by treatment in molten salt at 600 °C for 10 minutes and quenching in water for about 60 s or until the test rod could be touched by hand. Any remaining traces of salt were carefully removed from the whole test rod using 320 grit paper in a lathe at slow speed. The final polish of the middle section of the test rod, the section that will be exposed to the solution, was 600 grit paper, also in a lathe. Finally, the rods were degreased using ethanol and rinsed in deionized water immediately before mounting in the SSRT cell. Figure 2-1 shows the drawing for the test rods. Figure 2-2 shows the collection of nine test rods produced. Figure 2-2 also shows the approximate locations of O-rings that seal the inner test environment from the atmosphere. The lower O-ring is stationary, relative to the test cell and relative to the test rod. The upper O-ring is stationary relative to the test cell but moves relative to the test rod. The upper part of the test rod gradually slide through the O-ring, as the straining proceeds. More than one O-ring were frequently used for the upper as well as the lower end of the test rod.

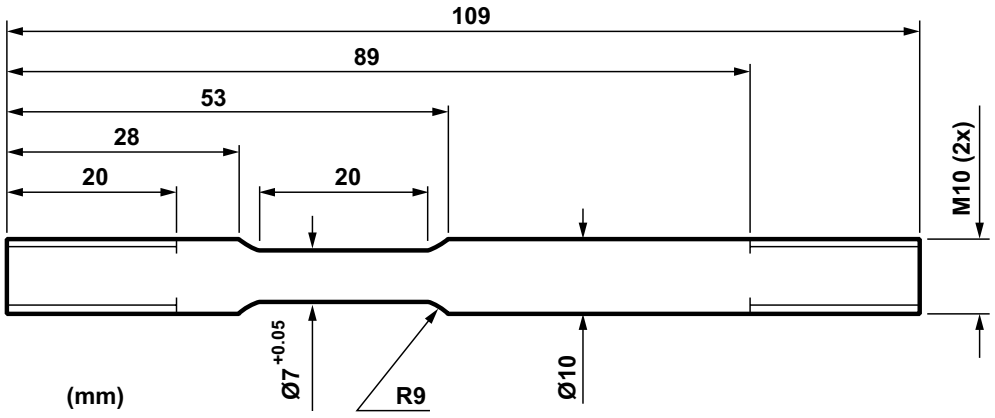

Figure 2-1. *Drawing for the test rods.*

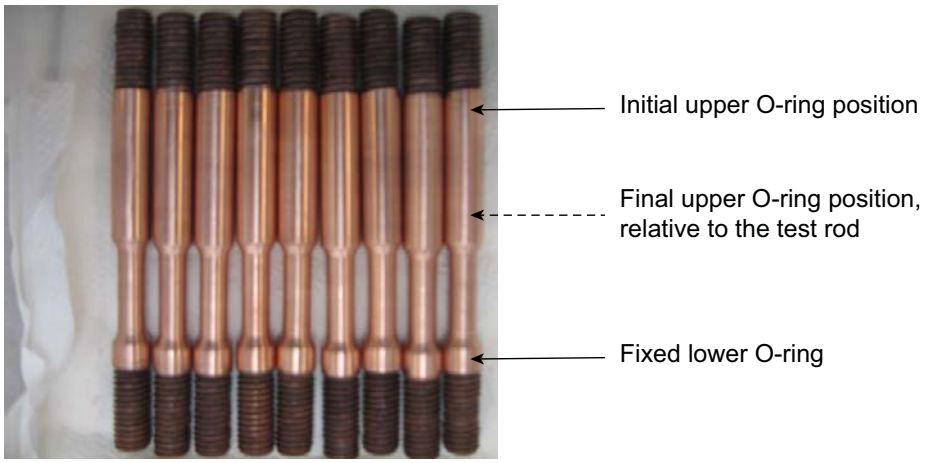

Figure 2-2. *The collection of nine test rods produced. Approximate locations of O-rings used to seal the inner test environment from the atmosphere are shown.*

2.2 Flow system

The experimental setup used was essentially the same as used in our previous study (Taxén et al. 2018). However, in the previous study only the sulfide stock solution was continuously fed through the SSRT-cell. In the present study, two stock solutions were fed by a tube pump. The alkaline sulfide stock solution was mixed with the pH 7.2 phosphate buffer solution in the SSRT-cell. The tube pump ensured that the two solutions were fed at the same rate. Figure 2-3 illustrates the experimental setup.

2.3 Stock solutions

Both stock solutions contained NaCl at the selected concentration. Na_2S was added to one of the stock solutions and a weighed amount of NaOH(s) to the other which was subsequently neutralized by phosphoric acid, H_3PO_4 to pH 7.2. Batches of 10 liters were prepared and for the tests to rupture which lasted about 14 days, the stock solution vessels were refilled once.

2.4 Slow strain rate testing

Figure 2-4 shows the SSRT-cell with a mounted test rod. The glass bulb to the lower left is a cell for the reference electrode which is kept at room temperature. The reference electrode is Ag/AgCl(sat. KCl), but the results are reported relative to the Saturated Calomel Electrode (SCE) subtracting a potential difference of 45 mV from the measured values (Bard and Faulkner 1980). The sampling valve is connected to the black tube and located just outside the lower left corner of the photograph. Figure 2-5 shows the parts when the cell is dismounted. Figure 2-6 shows the upper, moving end of the test rod and Figure 2-7 shows the lower, stationary end. The green O-rings mounted around each end of the test rod seal radially against a hole in the white Teflon cylinders.

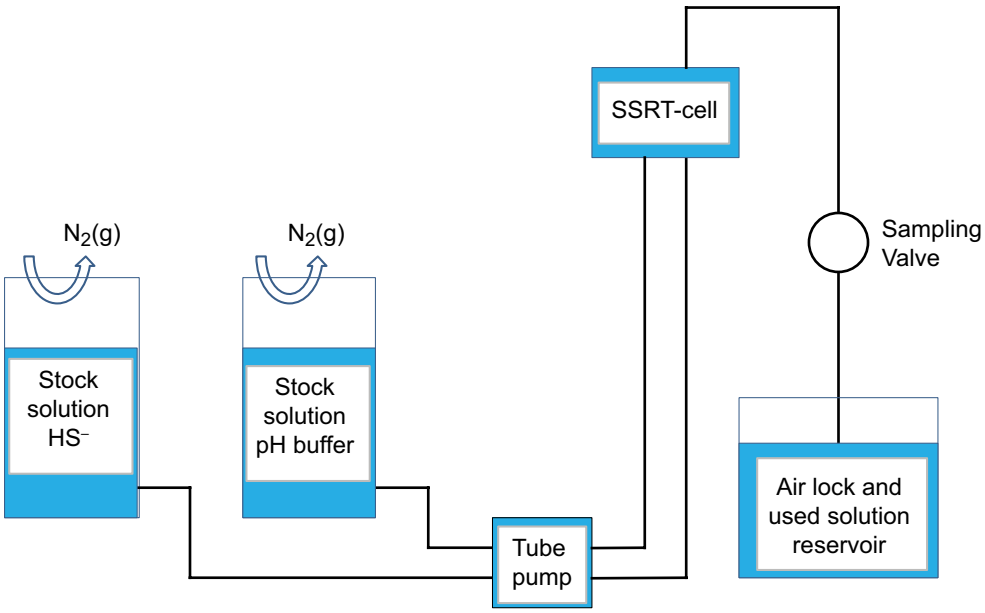

Figure 2-3. *Schematic sketch of the solution flow system during SSRT-test of copper.*

Figure 2-4. *Photograph of the SSRT-cell with a mounted test rod.*

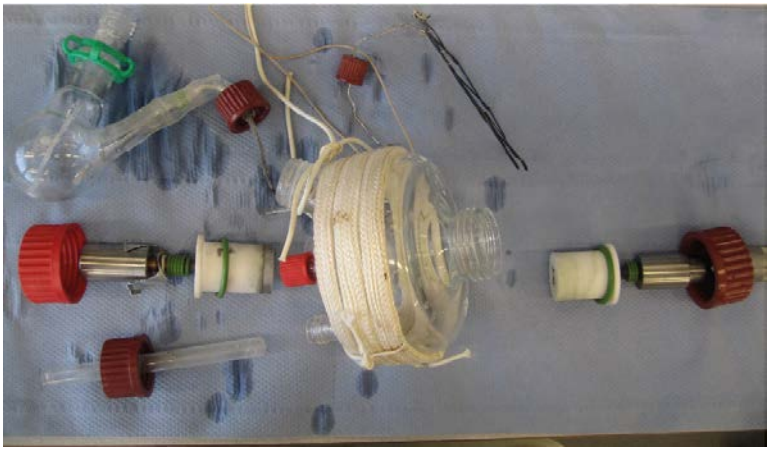

Figure 2-5. *Parts of the SSRT-cell, dismounted.*

Figure 2-6. *Parts of the SSRT-cell, dismounted. Upper, moving side of the test rod after testing.*

Figure 2-7. *Parts of the SSRT-cell, dismounted. Lower, stationary side of the test rod after testing.*

2.5 Stress and strain

Engineering stress and strain are reported, meaning that the stress and strain are related to the original shape of the test rod. The SSRT machine provides data for the applied force and for displacement. Force, F, and displacement, Δy, are recalculated into stress and strain, respectively.

$$Stress = \frac{F}{A_m}[\text{MPa}] \quad (2\text{-}1)$$

$$Strain = \frac{\Delta y}{L_a} \times 100\% \quad (2\text{-}2)$$

The average cross sectional area, A_m, is calculated from the average value of 5 readings of the diameter, d_m, of the narrow part of the test rod. The active length, L_a, is measured as the distance between the points where the diameter exceeds the average value, d_m+0.1 mm at each end of the narrow section.

2.6 Test matrix

Eight tests were performed. Table 2-1 summarizes the test conditions.

Table 2-1 Summary of the test conditions.

Run #	Temperature (°C)	Sulfide Concentration (mM)	(mg/L)	Chloride Concentration (mM)	Duration (days)
1	90	1	32	10	Until rupture
2	90	0.02	0.06	10	Until rupture
3	90	2	64	10	Until rupture
4	90	1	32	100	Until rupture
5	60	1	32	10	Until rupture
6	60	1	32	10	2
7	60	1	32	10	4
8	60	0.02	0.06	10	Until rupture

The extension rate was kept constant at 5×10^{-7} s^{-1}. Failure generally occurred after 14 days of strain, unless the test was interrupted. The solution contained a 10 mM phosphate buffer in all exposures.

The ninth produced test rod was analyzed for surface features without any exposure or testing in order to establish a base line.

2.7 Unloading procedure

For the interrupted tests, Run #6 and Run #7, the test rod was unloaded by reversing the SSRT machine so that the strain was reduced by the same rate, 5×10^{-7} s^{-1}, until the test rod could be removed. Unloading and removing usually took a few hours.

3 Results

3.1 Stress-strain curves

Figure 3-1 shows stress-strain curves for copper in near neutral solutions with sulfide and chloride. Section 2.5 describes how these parameters were calculated from measured quantities.

Figure 3-1 shows that the maximum stress applied to obtain the set strain rate is slightly lower at 90 °C than at 60 °C. Within each temperature, no significant influence of the composition of the test solution is seen. Final rupture occurs at a strain of about 80 % with a variation that is not uncommon in slow strain-rate tests.

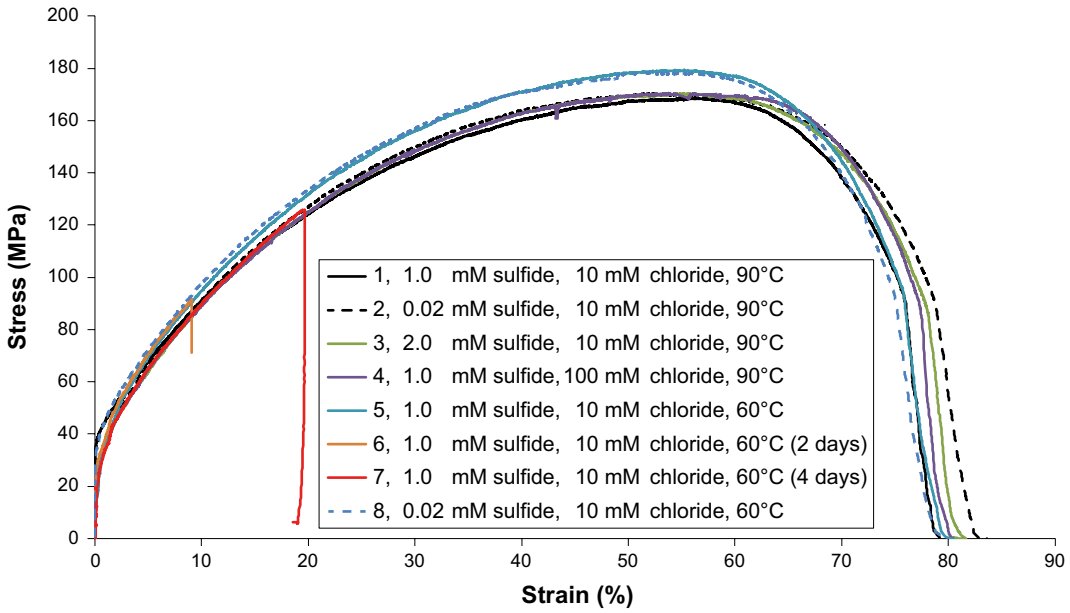

Figure 3-1. *Stress-strain curves for copper in near neutral solutions with sulfide and chloride.*

3.2 Corrosion potentials

Figure 3-2 shows the corrosion potential for the copper test rods and the potential for a platinum wire in the same solution. Figure 3-2 shows corrosion potentials of about –850 mV at 90 °C and at 60 °C for the higher sulfide concentrations (1 mM or 2 mM) but about –50 mV for 0.02 mM sulfide. The Pt-potentials are about 400 mM more positive than the corrosion potentials of copper, for the higher sulfide concentrations. The relatively high and increasing Pt-potential in Run #2 can be seen as an indication of oxygen influence in this experiment. However, all copper test rods turned black during the tests. A greenish spot on the test rod from Run #2 could be seen at a site where the O-rings around the test rod seal the test cell from the atmosphere. Green spots could be seen also on the test rod from Run #8. The green color indicates the presence of Cu(II) and oxidation by oxygen.

Table 3-1 shows calculated potentials for hydrogen evolution under some conditions relevant for the present study.

$$2H_2O + 2e^- \rightarrow H_2(g) + 2OH^- \qquad (3\text{-}1)$$

Table 3-1. Calculated potentials for hydrogen evolution at 1.0 atm under some conditions relevant for the present study. (V vs. SCE at room temperature)

Temperature °C	pH 7.2	pH 7.5
25	–0.67	–0.69
60	–0.69	–0.71
90	–0.72	–0.74

A value of 0.242 was used to convert potentials from the hydrogen scale to the SCE-scale at room temperature (Bard and Faulkner 1980). Thermodynamic data for $H_2(g)$ in Puigdomenech and Taxén (2000) was used.

Comparing the values in Table 3-1 with the corrosion potentials for copper in Figure 3-2, it is evident that hydrogen evolving corrosion was possible in all experiments with 1 mM sulfide but not with 0.02 mM sulfide. The corrosion observed with this low sulfide concentration also resulted in a black corrosion product, with the appearance of $Cu_2S(s)$, that covered the test rods.

But the cathodic reaction was probably driven by oxygen leaking from the atmosphere.

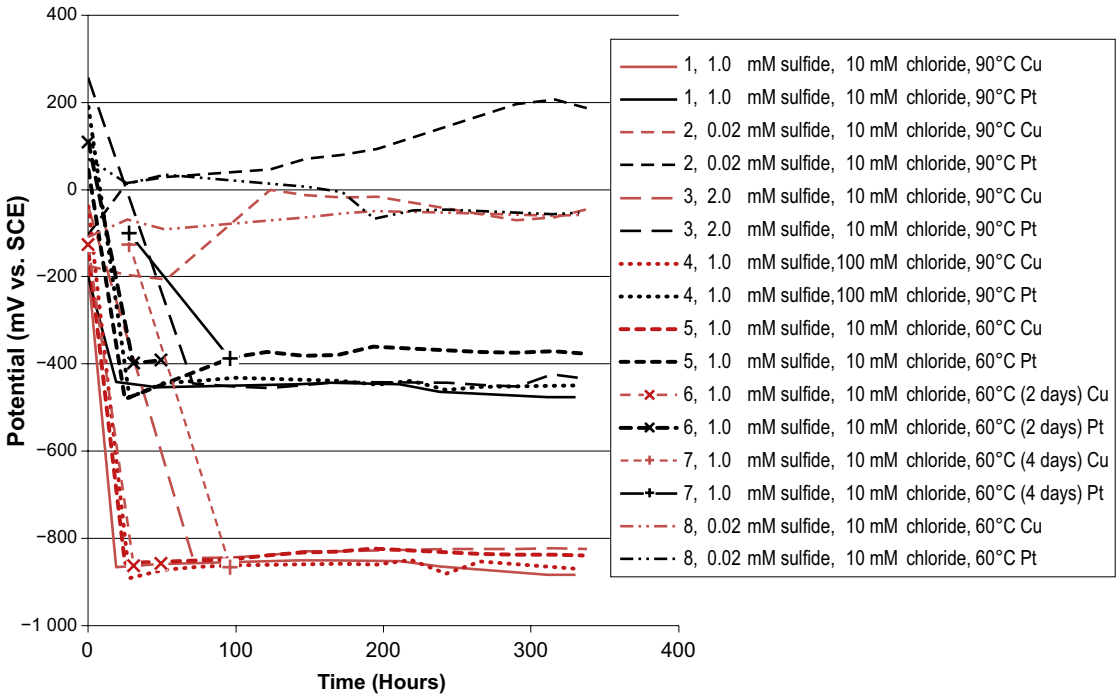

Figure 3-2. *The corrosion potential for the copper test rods (red curves) and the potential for a platinum wire (black curves) in the same solution.*

3.3 Sulfide

Figure 3-3 shows the sulfide concentrations measured in solution from the cell. The error bars are constructed from the color standards for the visual analysis.

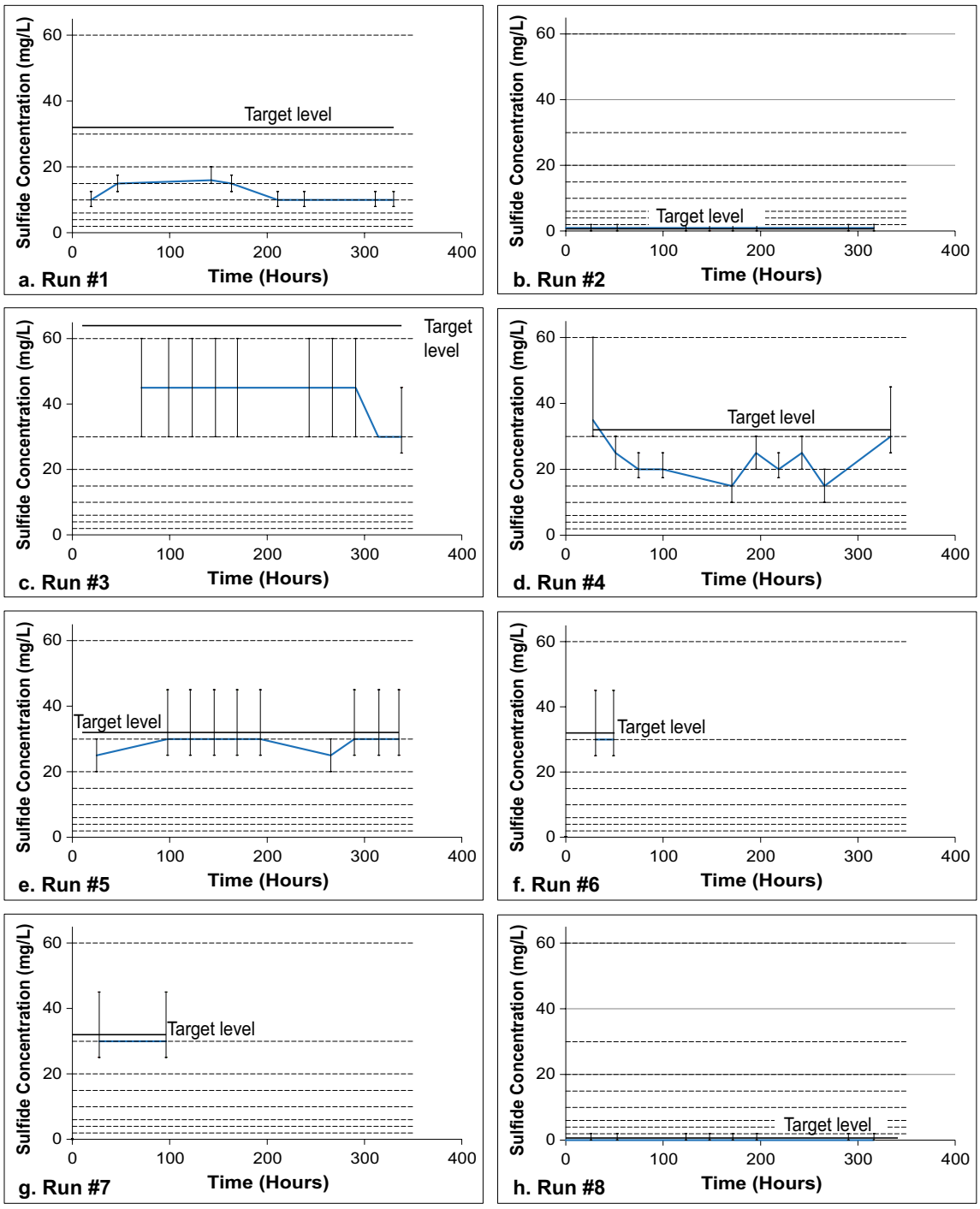

Figure 3-3. *Sulfide concentrations measured in solution from the cell. The dashed lines indicate the sulfide levels for the color standards. Kindly note that the error bars include only the possible errors from comparisons of the sample color to the color standards. There is also an error caused by the delay between sampling and analysis.*

3.4 pH

Figure 3-4 shows the pH measured in solution from the cell. Figure 3-4 shows that there were some variations in pH during experiments and between experiments. The 10 mM phosphate pH-buffer was apparently not sufficient to fully neutralize the alkalization from the sulfide stock solution. The influence of the corrosion process on the pH can probably be neglected. Runs #2 and #8, with the low sulfide concentration, show small deviations from the buffer of pH 7.2.

3.5 Metallographic examinations

A large number of images were taken using both Light Optical Microscopy (LOM) and Scanning Electron Microscopy (SEM) for all the test rods examined. SEM-images of longitudinal cross sections seem to be a sensitive method for detecting cracks or crack-like features. Depths of penetration could also be estimated from such images.

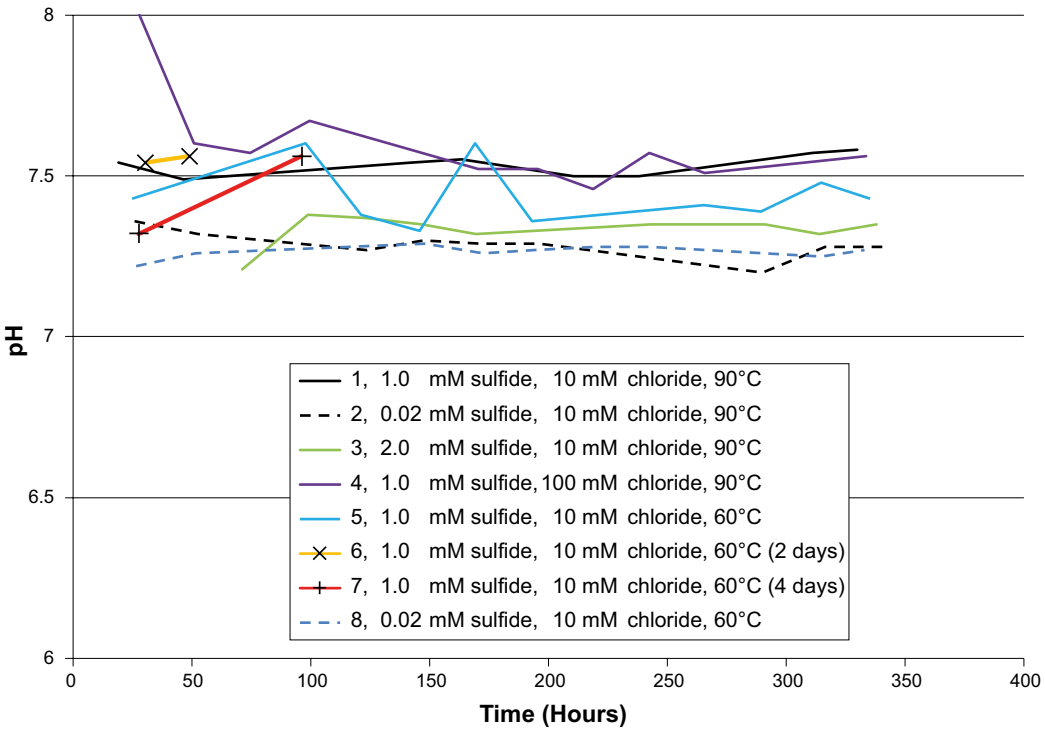

Figure 3-4. *pH measured in the solutions from the cell.*

3.5.1 Run #1, 1 mM sulfide, 10 mM chloride, 90 °C with Run #2, 0.02 mM sulfide as reference

Figure 3-5 shows a sequence of SEM-images of longitudinal cross sections of test rods from Run #1 in the left hand column with similar images from Run #2, for comparison, in the right hand column.

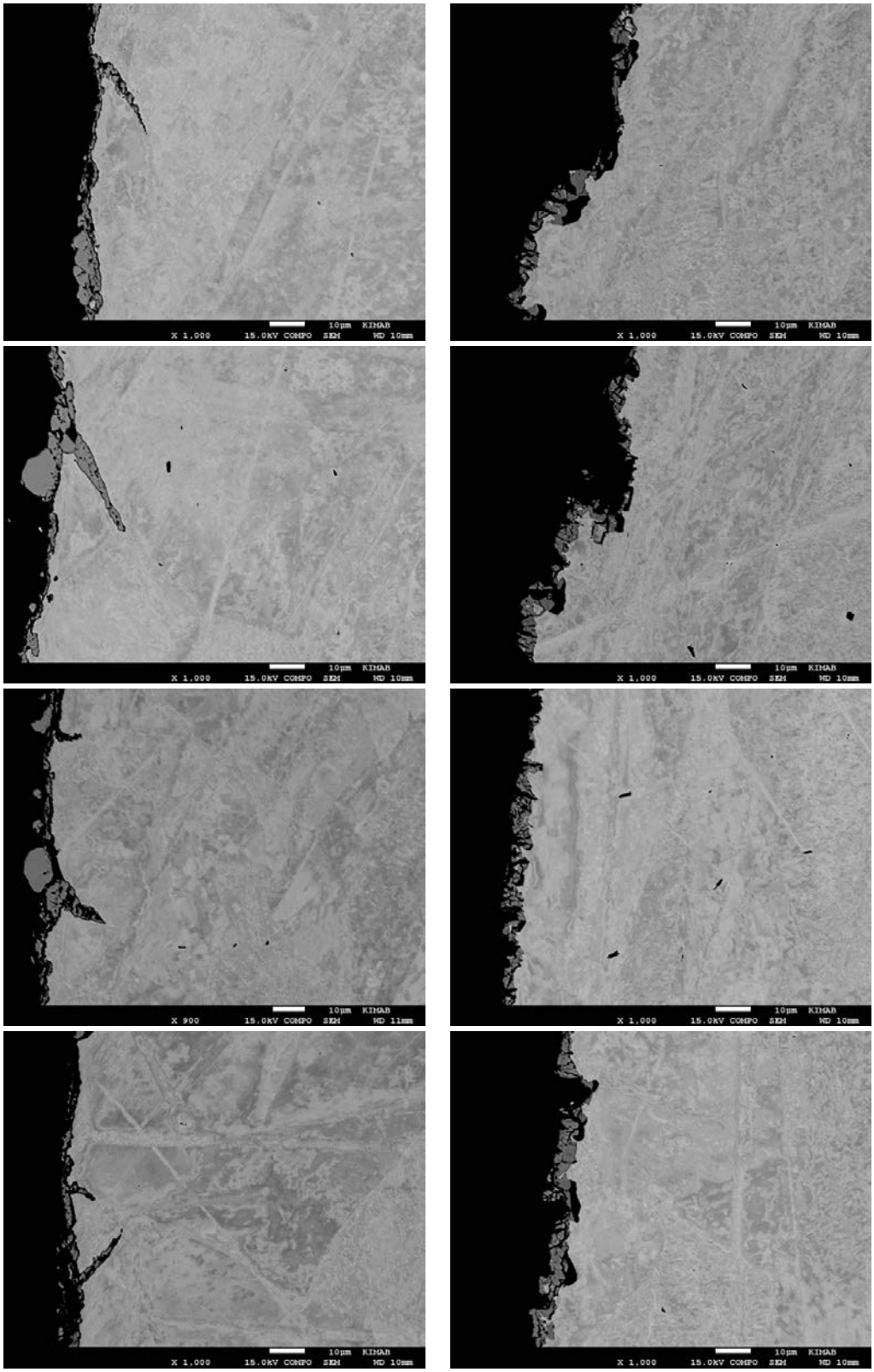

Run #1. 1 mM sulfide, 10 mM chloride, 90°C **Run #2. 0.02 mM sulfide, 10 mM chloride, 90°C**

Figure 3-5. *SEM-images of longitudinal cross sections of test rod from Run #1 in the left hand column with similar images from Run #2 in the right hand column for comparison.*

The images in the left hand column of Figure 3-5 show cracks or crack-like features that extend to about 20–30 µm from the surface. The images in the right hand column show no such cracks but only an unevenly corroded surface. Figure 3-6 shows the approximate distribution of cracks along the longitudinal cross section of one of the halves of the test rod from Run #1.

3.5.2 Run #3, 2 mM sulfide, 10 mM chloride, 90 °C, to rupture

Figure 3-7 shows a SEM-image of the cross section of the test rod from Run #3, with 2 mM sulfide instead of 1 mM in Run #1.

It was noted that the cross section of the test rod showed cracks of similar depth as Run#1 but the cracks were fewer and generally notably wider. One exception is the thin crack to the left of the large, wide crack in the right image in Figure 3-7.

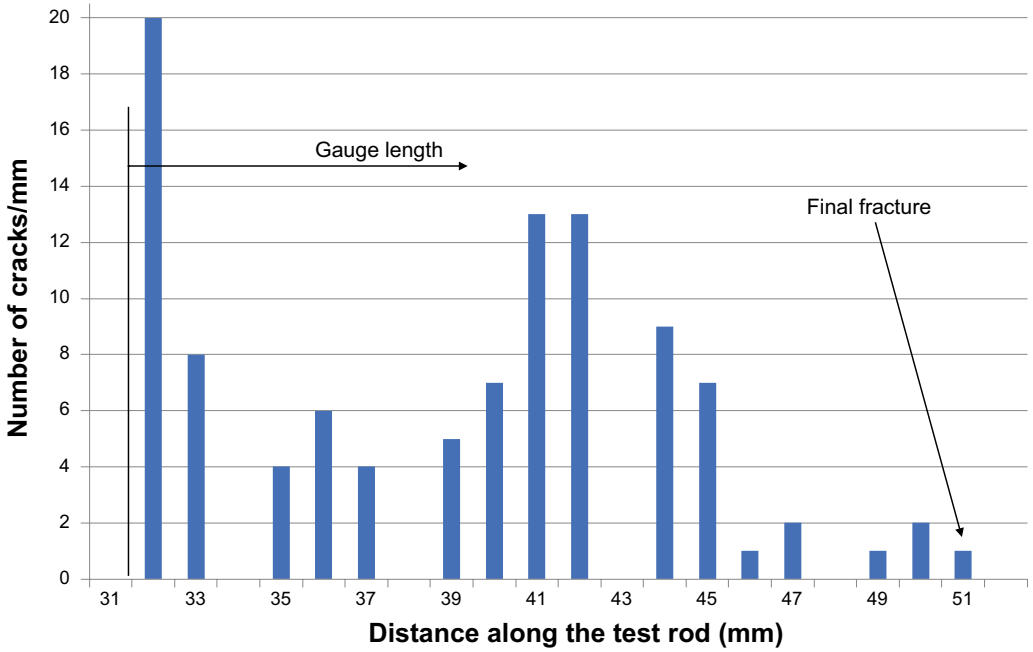

Figure 3-6. *Approximate distribution of cracks along the longitudinal cross section of one of the halves of the test rod from Run #1 (1 mM sulfide, 10 mM chloride, 90 °C).*

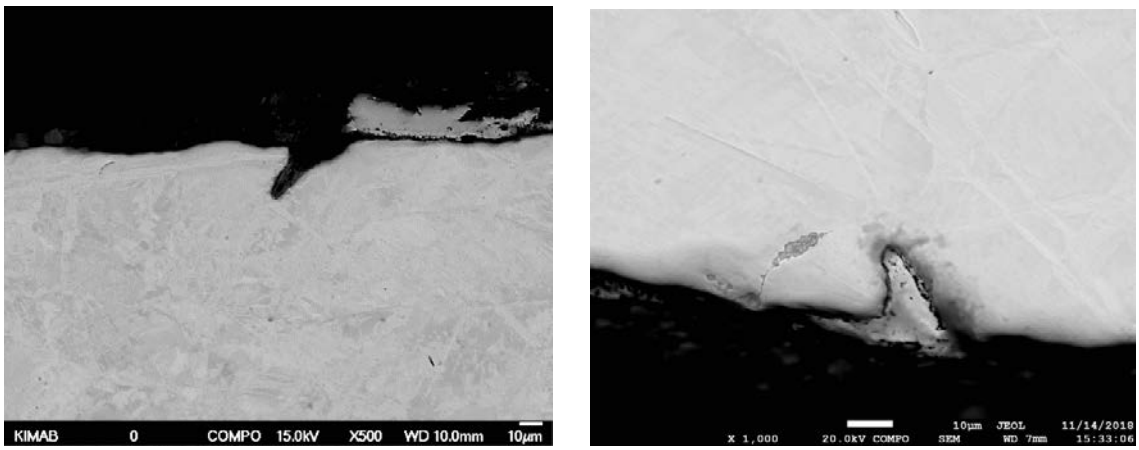

Figure 3-7. *SEM-images of the cross section of the test rod from Run #3, (2 mM sulfide, 10 mM chloride, 90 °C).*

3.5.3 Run #4, 1 mM sulfide, 100 mM chloride, 90 °C, to rupture

Figure 3-8 shows SEM-images of the cross section of the test rod from Run#4, with 1 mM sulfide and 100 mM chloride. The right hand image shows a magnification of the middle part of the left hand image. The shapes of the cracks are generally more similar to the relatively wide cracks found for Run #3 than the more narrow cracks from Run #1. However, the lower images in Figure 3-8 show an example of a deep lying fine structure of a crack. Just as in Run#3, there were fewer cracks in Run #4 than in Run #1.

The images from Run #4, with 100 mM chloride, in Figure 3-8, show much more solid corrosion products than the images from Run #1, with 10 mM chloride, in Figure 3-5.

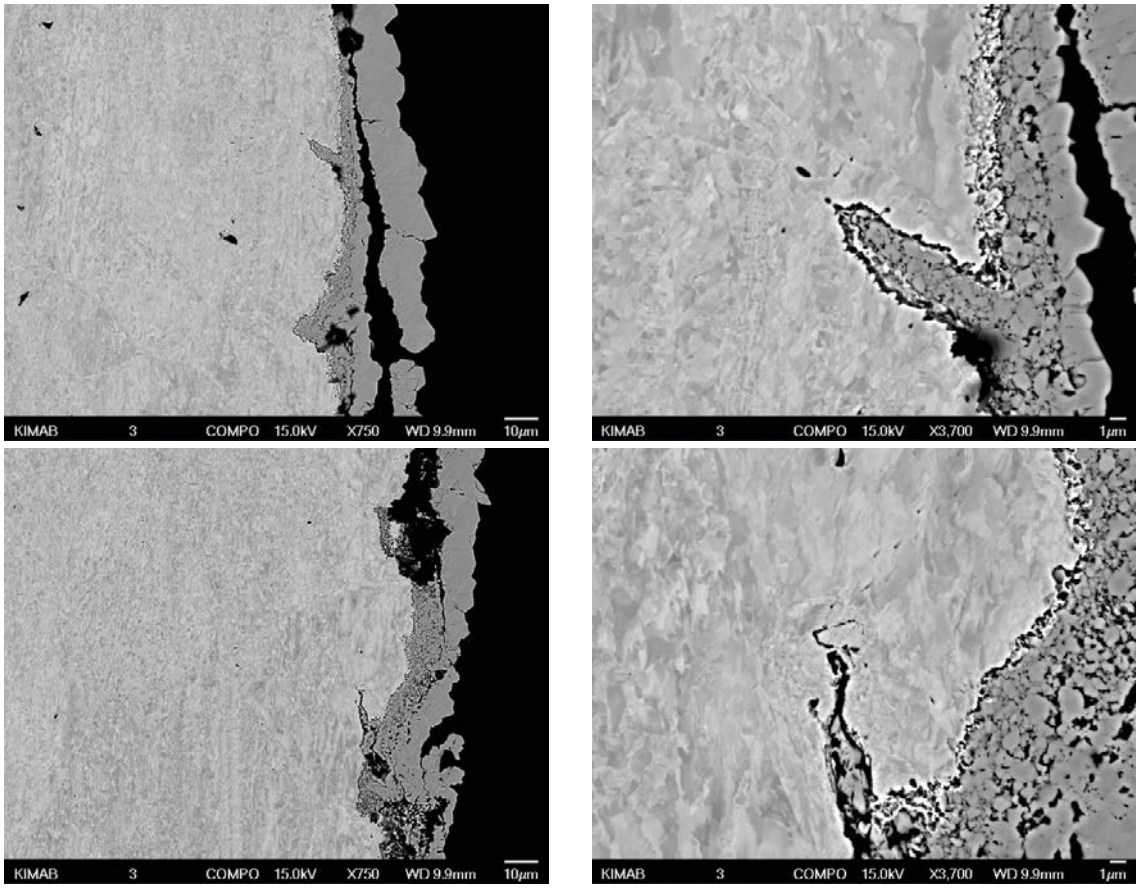

Figure 3-8. *SEM-image of the cross section of the test rod from Run #4, (1 mM sulfide, 100 mM chloride, 90 °C). The upper right image shows a magnification of the middle part of the left image. The lower right image shows a magnification of the middle part of the left image.*

3.5.4 Run #5, 1 mM sulfide, 10 mM chloride, 60 °C, to rupture

Figure 3-9 shows photographs of one end of the test rod strained to rupture in Run #5, which was similar to Run #1 but at 60 °C instead of 90 °C.

The final rupture appeared at the middle of the gauge section, approximately. This was found also for previous runs. The axial photo of the rupture reveals a hexagonal profile which was not found in the other experiments where the axial profiles were more rounded in shape but with irregular edges. The straight looking edges extending for about 1 mm in Figure 3-9 suggest a correlation between the site of final rupture and previous surface cracks. Without previous surface cracks, the profile of the fracture would probably have been more irregular in shape.

Figure 3-10 shows some SEM-images from Run#5. The left hand image in Figure 3-10 shows an uneven surface profile which at closer inspection is found to contain a large number of cracks. The maximum depth of the cracks is about 10–20 µm which is similar to or slightly shorter than what was found in Run #1 at 90 °C.

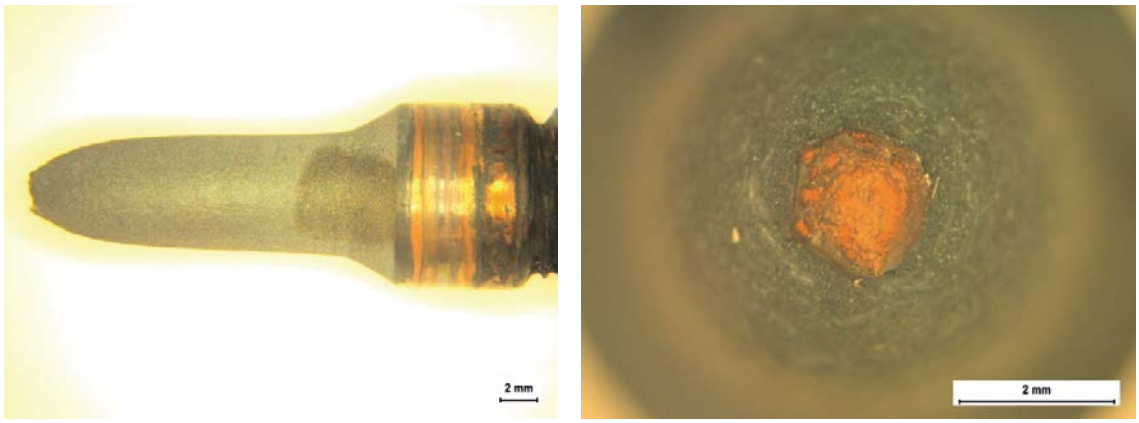

Figure 3-9. *Photographs of one end of the test rod strained to rupture in Run #5 (1 mM sulfide, 10 mM chloride, 60 °C).*

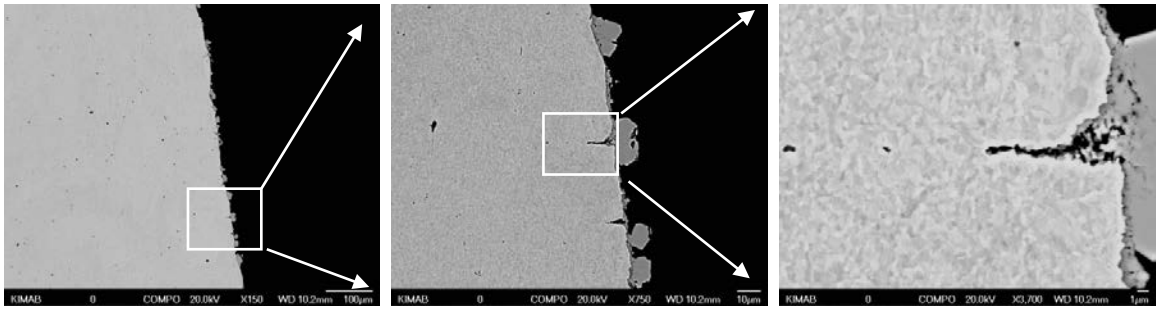

Figure 3-10. *A sequence of SEM-images in gradually increasing magnification. Run #5, (1 mM sulfide, 10 mM chloride, 60 °C).*

3.5.5 Run #6, 1 mM sulfide, 10 mM chloride, 60 °C, 2 days

In Run #6 the SSRT-test was interrupted after 2 days of elongation. Figure 3-11 shows a photo of the test rod from Run #6.

Figure 3-11 shows that the whole exposed section of the test rod has acquired a blackish color, presumably from copper sulfide. There is an apparent difference in brightness. While most of the test rod is dull, there is a patch towards the *B-C* end of the test rod where the surface is much brighter while still blackish.

SEM analysis of the longitudinal cross section revealed a number of cracks where the crack density could be correlated with the longitudinal location. Figure 3-12 shows a histogram for the number of cracks found. Figure 3-12 shows that the *A-D* end of the test rod had more cracks than the *B-C* end and that no cracks were found in the middle portion of the test rod.

Figure 3-13 shows representative images from positions *A* through *D* in Figure 3-11. Figure 3-13 shows that the maximum depth of the cracks is in the order of 10 µm.

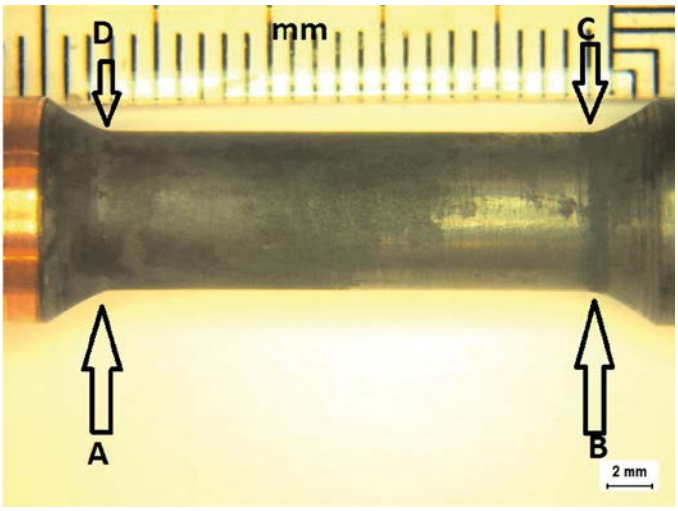

Figure 3-11. *Photo of the test rod from Run#6 (1 mM sulfide, 10 mM chloride, 60 °C, 2 days). A ruler with mm scale is included, and the four positions where the diameter of the rod gradually increases are denoted by letters.*

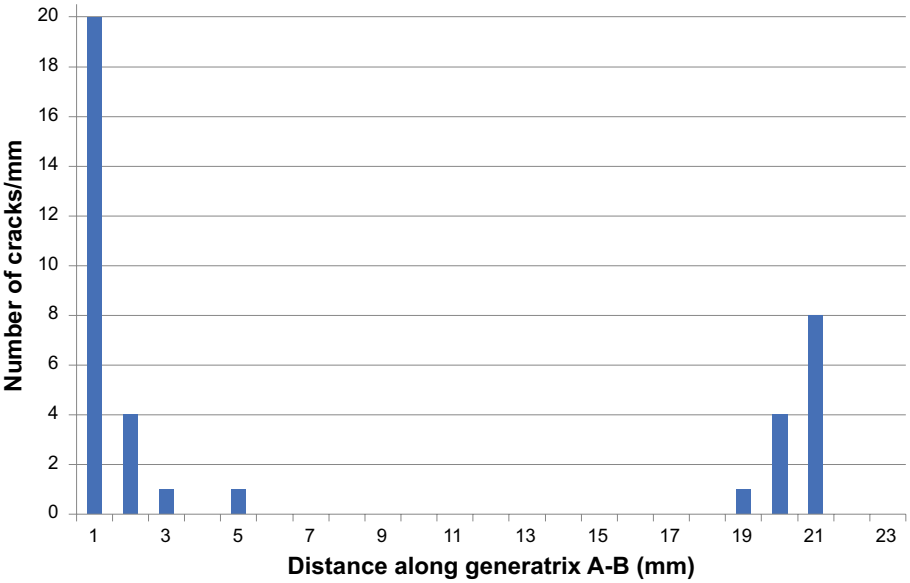

Figure 3-12. *Histogram for the number of cracks found at various locations at the test rod in Figure 3-11. The longitudinal cross section was studied (Run #6, 1 mM sulfide, 10 mM chloride, 60 °C, 2 days).*

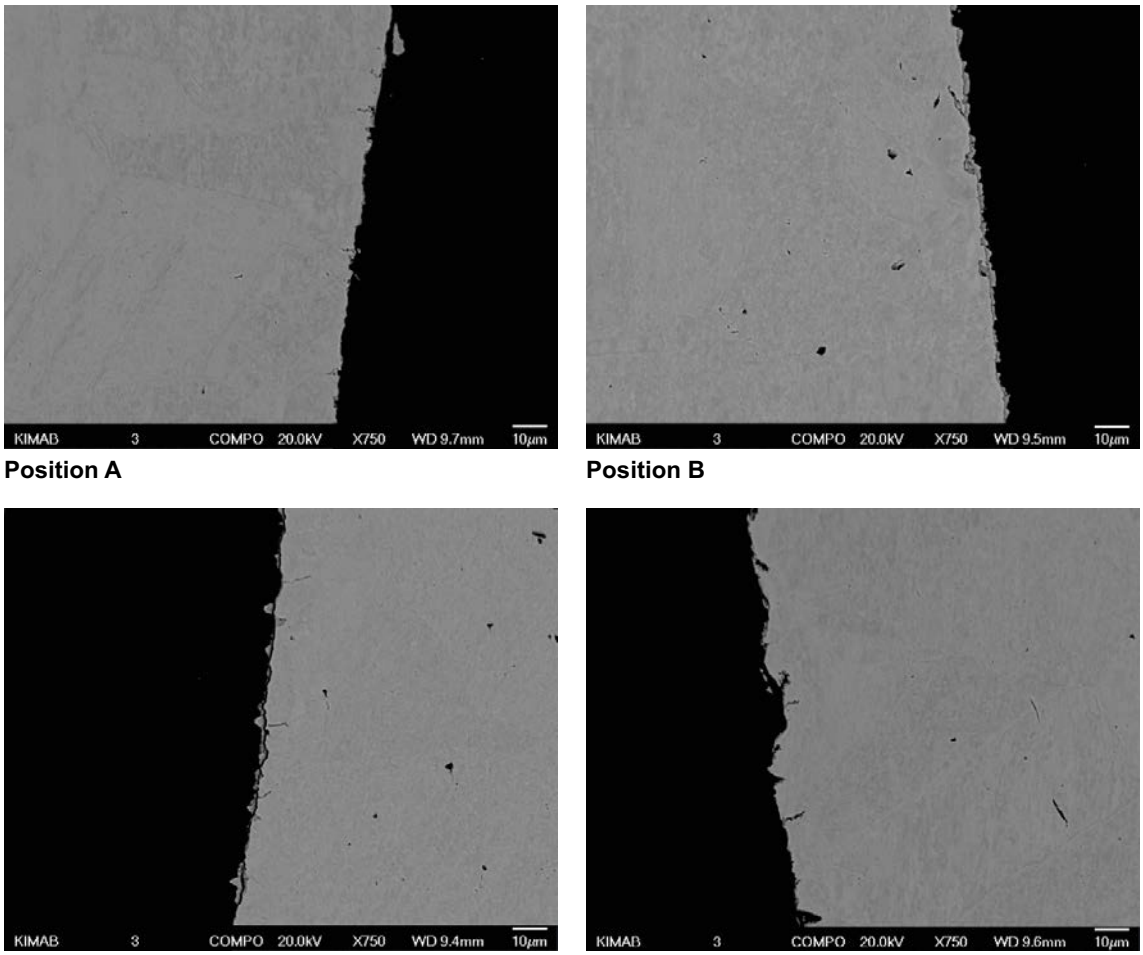

Figure 3-13. *Representative images from positions A through D in Figure 3-11 (Run #6, 1 mM sulfide, 10 mM chloride, 60 °C, 2 days).*

3.5.6 Run #7, 1 mM sulfide, 10 mM chloride, 60 °C, 4 days

In Run #7 the SSRT-test was interrupted after 4 days of elongation. Figure 3-14 shows a photo of the test rod from Run #7.

The test rod in Figure 3-14 has a more evenly dull appearance than in Figure 3-11 although some more shiny spots are visible also in Figure 3-14.

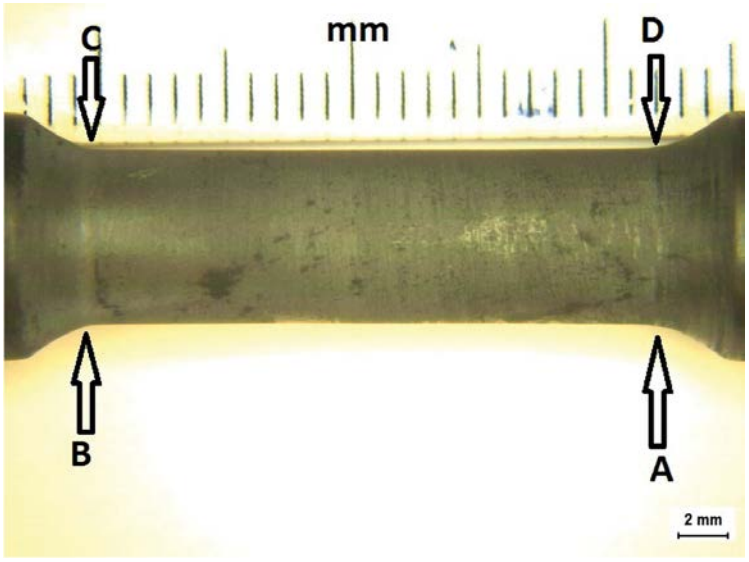

Figure 3-14. *Photo of the test rod from Run#7. A ruler with mm scale is included, and two positions where the diameter of the rod gradually increases are denoted by letters (Run #7, 1 mM sulfide, 10 mM chloride, 60 °C, 4 days).*

Figure 3-15 shows histograms for the number of cracks found after Run #7.

Comparing the histograms in Figure 3-15 with similar data in Figure 3-12, Figure 3-15 shows a similar concentration of cracks at positions *A*, *B*, *C* and *D*. However, the distribution of cracks is a bit more even in Figure 3-15 compared to Figure 3-12 and there are some cracks also close to the middle of the test rod.

Figure 3-16 shows representative images of the polished longitudinal cross section from positions *A* through *D* in Figure 3-14.

The maximum depth of penetration is in the order of 10 µm after four days of exposure. This is not significantly different from 10 µm estimated from Run #6 after two days of exposure. At failure, after 14 days of exposure in Run #5, the maximum depth of penetration was estimated to 10–20 µm.

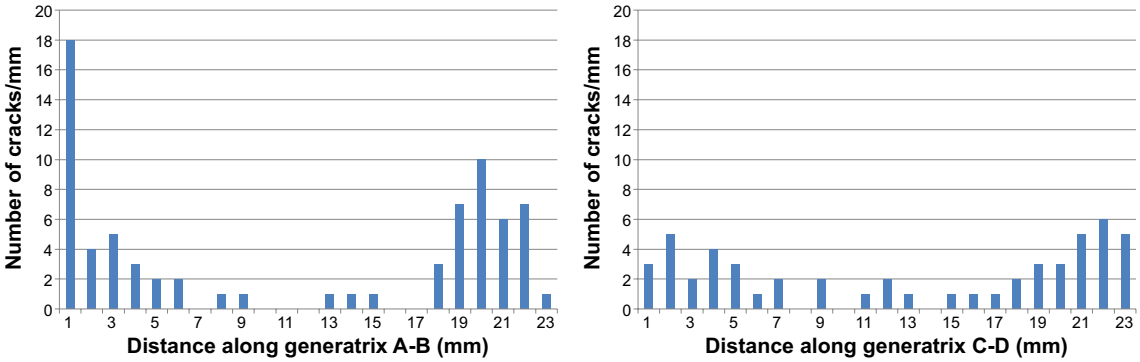

Figure 3-15. *Histograms for the number of cracks found at various locations at the test rod in Figure 3-14. The longitudinal cross section was studied along generatrix A-B (left) and C-D (right), from Figure 3-14 (Run #7, 1 mM sulfide, 10 mM chloride, 60 °C, 4 days).*

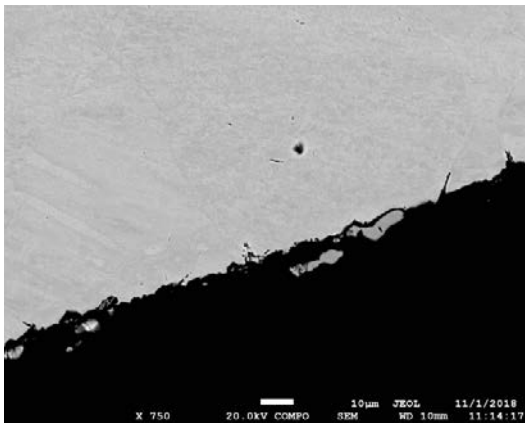

Position A

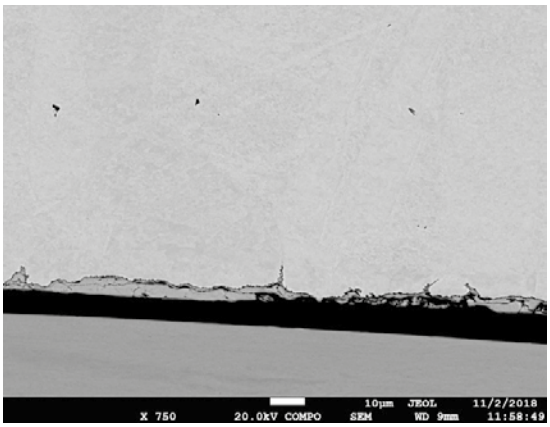

Position B

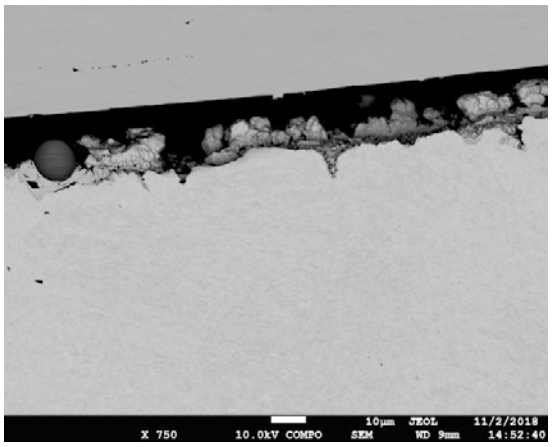

Position C

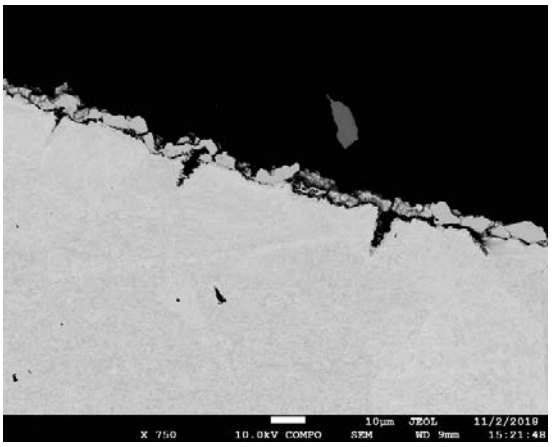

Position D

Figure 3-16. *Representative images of the polished longitudinal cross section from positions A through D in Figure 3-14 (Run #7, 1 mM sulfide, 10 mM chloride, 60 °C, 4 days).*

3.5.7 Run #8, 0.02 mM sulfide, 10 mM chloride, 60 °C, to rupture

The test rod from Run #8 was black but showed spots with a clear greenish color after testing which indicates an influence of oxygen and the formation of Cu(II). Figure 3-17 shows a collection of four SEM-images of the polished longitudinal cross section of the test rod in Run #8.

The surface profiles in Figure 3-17 are similar to those found after Run #2 in the right column of Figure 3-5. No cracks or crack-like features are found but an unevenly corroded surface with loosely attached corrosion products.

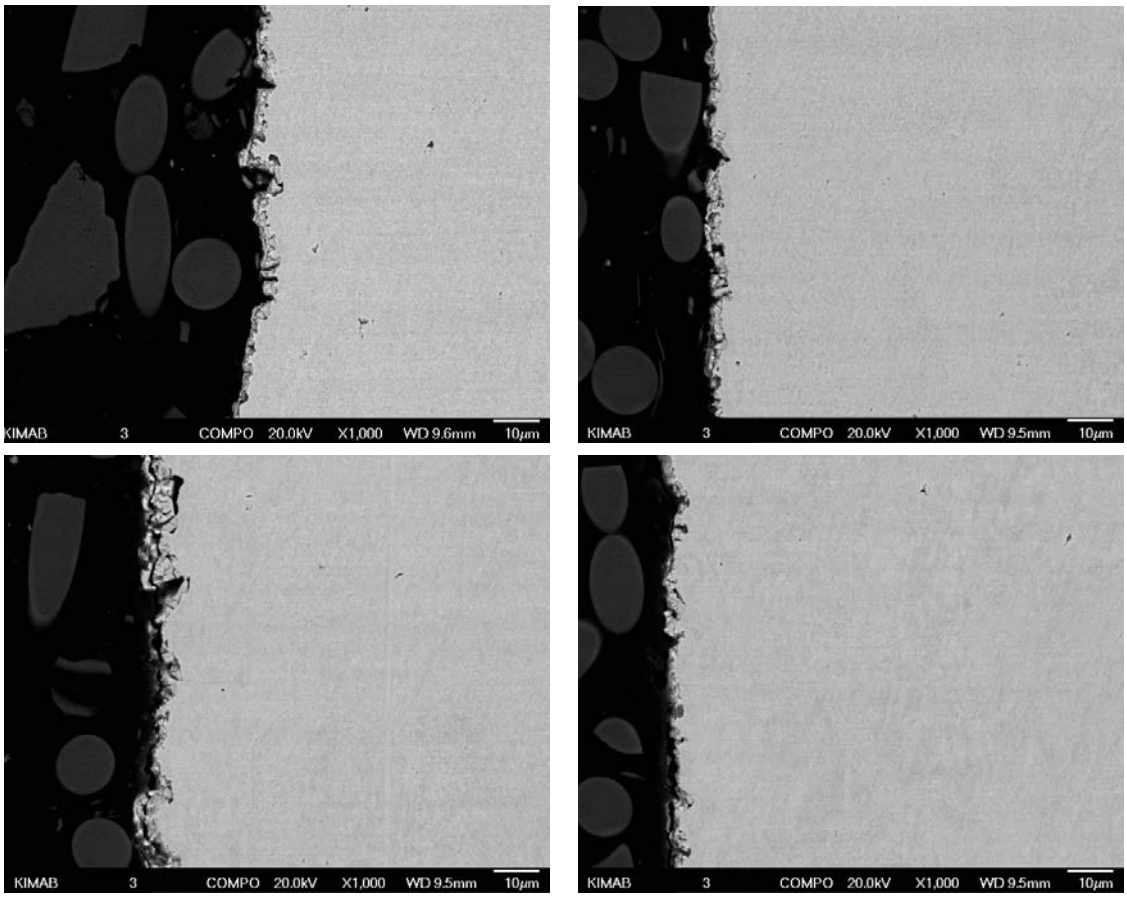

Figure 3-17. *A collection of four SEM-images of the polished longitudinal cross section of the test rod in Run #8 (0.02 mM sulfide, 10 mM chloride, 60 °C).*

3.5.8 Unexposed test rod

One unexposed test rod was also subjected to metallographic examination. Figures 3-18 and 3-19 shows photographs of the test rod.

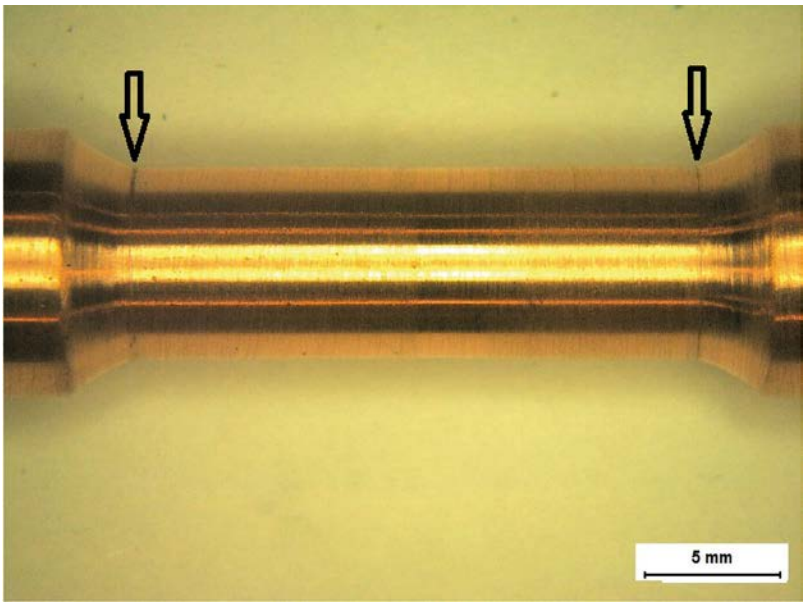

Figure 3-18. *Photograph of an unexposed test rod. The arrows indicate circular patches at the border between the gauge length and the transition radius.*

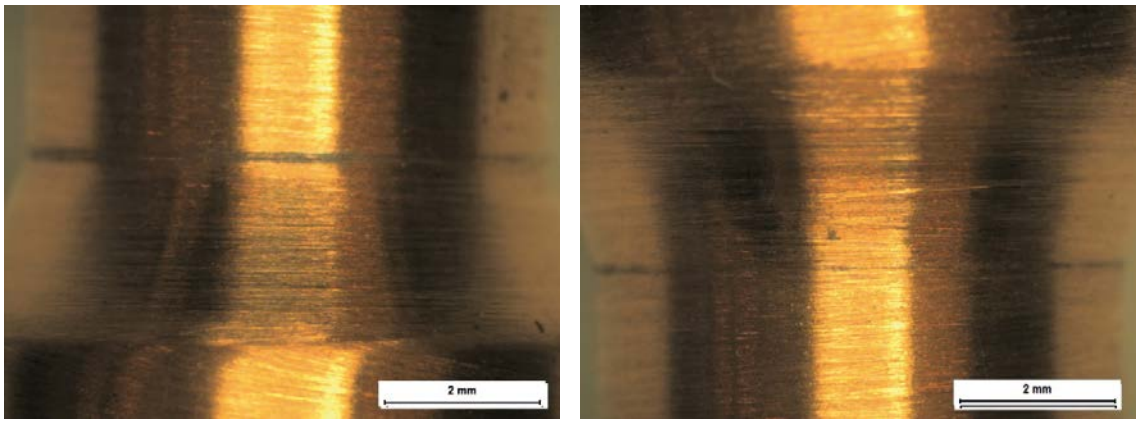

Figure 3-19. *Details from Figure 3-18. Borders between the gauge length and the transition radius. Left and right, respectively (unexposed test rod).*

SEM images of the longitudinal cross section are shown in Figure 3-20 and in greater detail in Figure 3-21. The images in Figure 3-21 show that there are material defects in the test rod. Some defects are fully enclosed by copper while other extend to the surface.

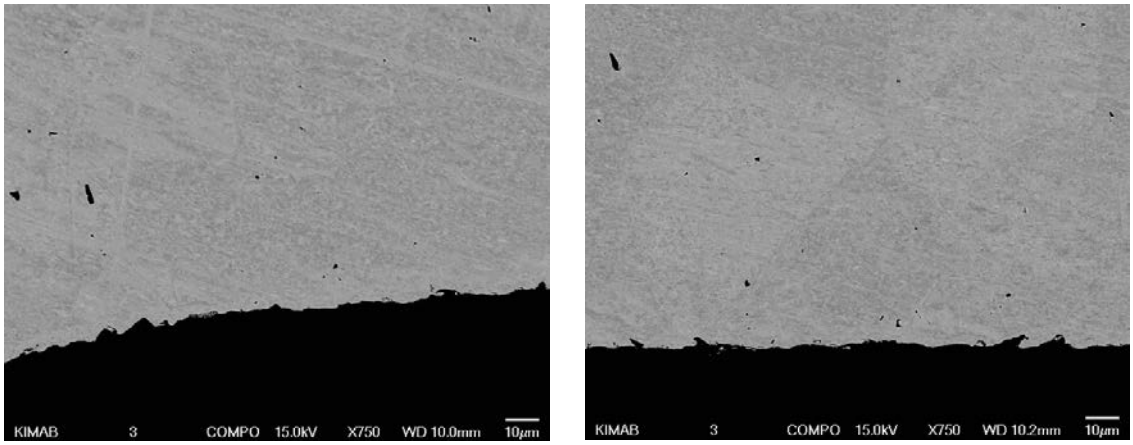

Detail of the transition radius. **Detail of the surface of the gauge length.**

Figure 3-20. *SEM-images of a longitudinal cross section of an unexposed test rod.*

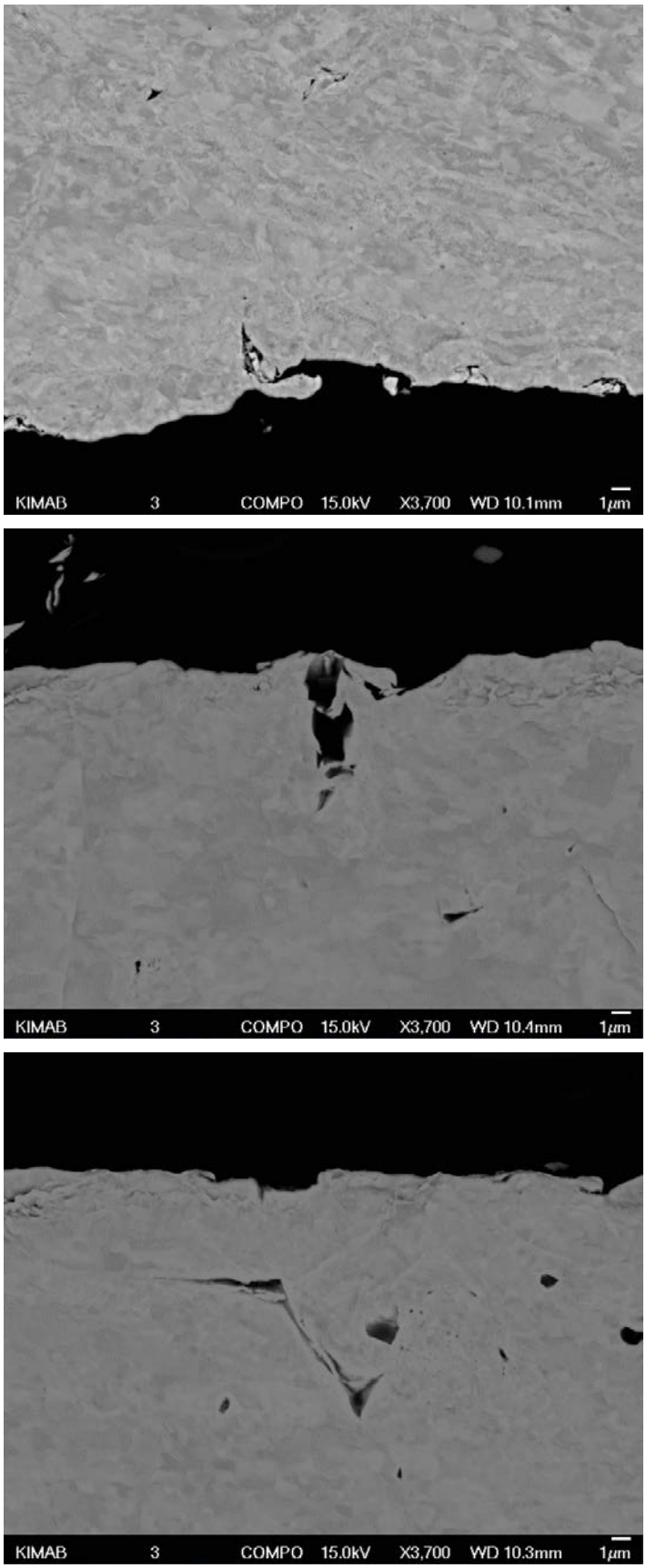

Figure 3-21. *Set of three images of material imperfections found in a cross section of the unexposed test rod.*

3.6 Element analyses

Run #1, 1 mM sulfide, 10 mM chloride, 90 °C

Figure 3-22 shows a back scatter image from Run #1. An intercrystalline crack is visible to a depth of about 10 µm. Figure 3-23 shows a line analysis for sulfur, oxygen and chlorine along the white line. The width of the sulfur band is about 0.8 µm. The line analyses also revealed the presence of oxygen along the line also outside the apparent boundaries of the crack but at a slightly higher concentration in the crack. A small peak for chlorine was detected in the crack.

Run #2, 0.02 mM sulfide, 10 mM chloride, 90 °C

Figure 3-24 shows a SEM image of the outer surface of the test rod from Run #2. The locations for three areas of analyses are shown. The element analyses are also shown.

Figure 3-24 indicates that the layer contains mostly oxygen, carbon and sulphur. Spectrum 7, seemingly located at a bare spot, reveals relatively small amounts of carbon and oxygen, along with copper. Notably, a relatively high concentration of phosphorus was found in the two locations with adherent scale.

Run #3, 2 mM sulfide, 10 mM chloride, 90 °C

Figure 3-25 shows an image of the thin crack in the right image of Figure 3-7. Figure 3-26 shows the element analyses along the Line Data 1.

Figure 3-26 shows that oxygen is a dominating element, after copper, at the location of Line Data 1.

Run #4, 1 mM sulfide, 100 mM chloride, 90 °C

Figure 3-27 shows an image of the polished longitudinal cross section of the test rod from Run #4.

The image in Figure 3-27 shows what appears to be two distinct layers of corrosion products with very similar compositions. The outer layer appears more crystalline or at least more dense and the inner layer seems more porous. The layers of corrosion products are much thicker than for the previous runs, at least the corrosion products that adhere to the copper surface. This was observed also in Figure 3-8 from the same test rod.

Run #5, 1 mM sulfide, 10 mM chloride, 60 °C

Figure 3-28 shows a SEM image of the test rod from Run #5. The fracture zone is seen to the left and the outer surface to the right. The locations for three areas of analyses are shown. The element analyses are also shown.

The image shows that the surface concentration of sulfur depends strongly on the location. The sulfur content is significantly higher at the outer surface than at the fracture zone and the deeper into the fracture zone, the lower the sulfur content. The fracture zone has the dimpled appearance associated with ductile fracture.

Run #6, 1 mM sulfide, 10 mM chloride, 60 °C, 2 days

Figure 3-29 shows an image of the central part of the test rod from Run #6. The locations for three areas of analyses are shown. The element analyses are also shown.

Figure 3-29 shows that there are scratch marks on the surface and that these areas are associated with elevated concentrations of carbon and silicon. Calcium is found in the deep groove at Spectrum 1.

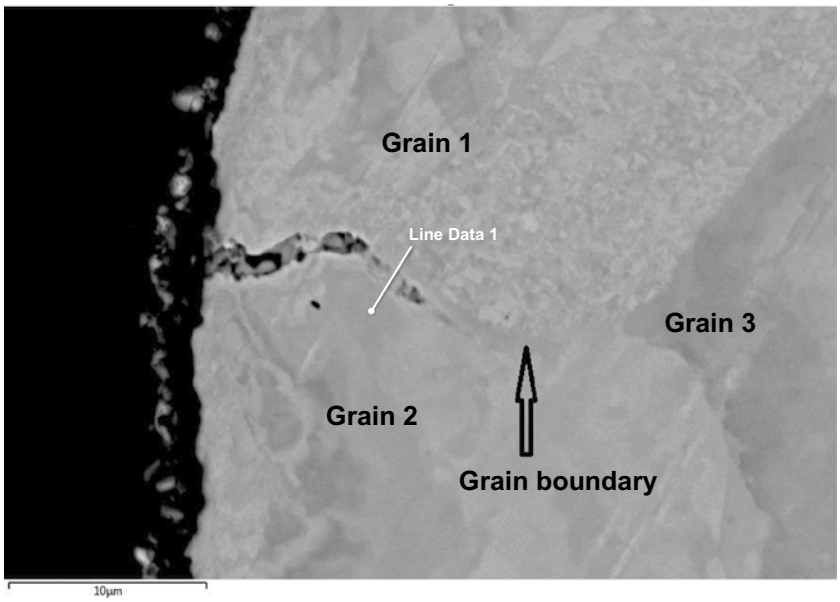

Figure 3-22. *A back scatter image of the test rod from Run #1. Three distinct grains are labelled and the grain boundary along which a crack seems to have developed. The location of a line analysis is also labelled (Run #1, 1 mM sulfide, 10 mM chloride, 90 °C).*

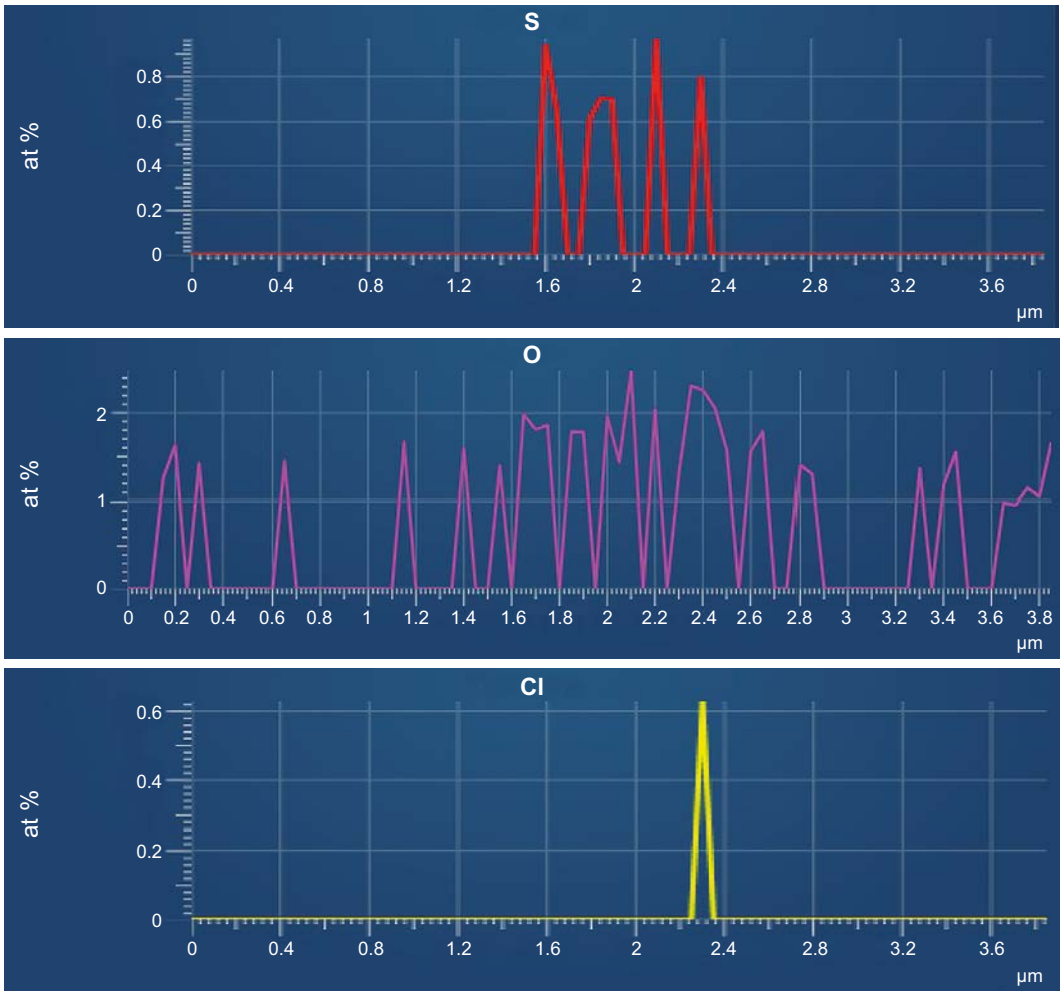

Figure 3-23. *Line analysis for sulphur, oxygen and chlorine along the line in Figure 3-22.*

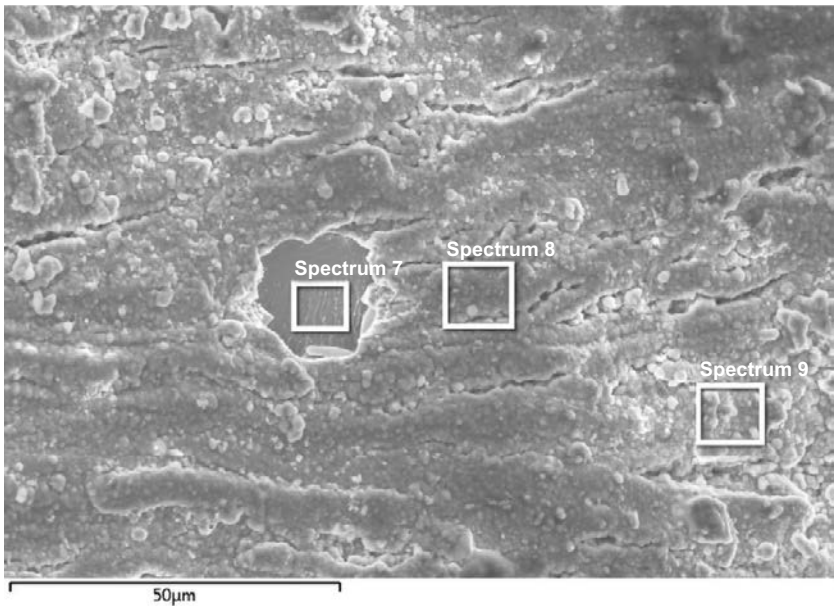

Spectrum Label	C	O	Al	Si	P	S	Cl	Ca	Fe	Cu	Tot
Spectrum 7	7.41	8.02	0	0.26	0.27	0	0	0	0	84.03	100
Spectrum 8	13.28	55.29	1.21	0.1	10.07	3.42	0.13	0.7	0.21	15.59	100
Spectrum 9	16.61	51.46	0.95	0.26	9.98	3.83	0.12	0.84	0.15	15.8	100

Figure 3-24. *SEM image of the test rod from Run #2. The locations for three areas of analyses are shown. The element analyses (in at %) are also shown (Run #2, 0.02 mM sulfide, 10 mM chloride, 90 °C).*

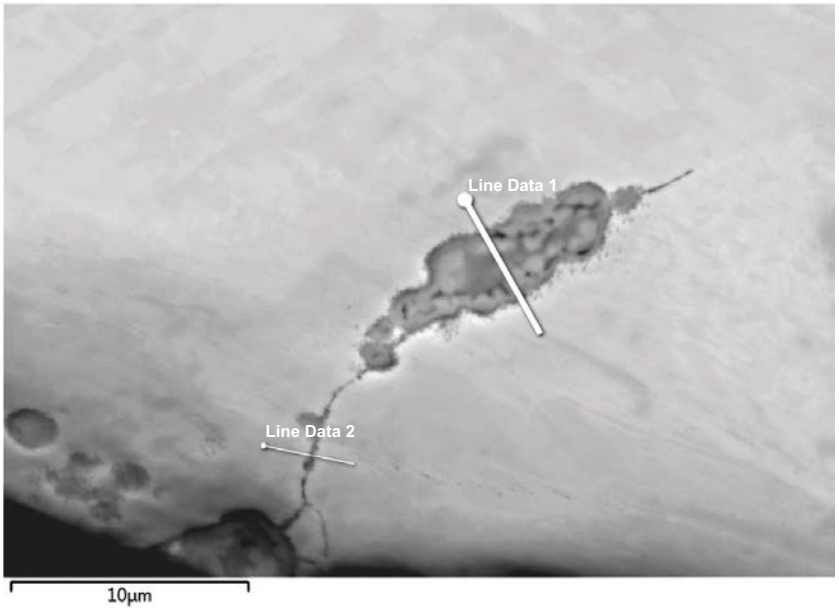

Figure 3-25. *Image of the thin crack in the right image of Figure 3-7. The curves show the element analyses along the Line Data 1 (Run #3, 2 mM sulfide, 10 mM chloride, 90 °C).*

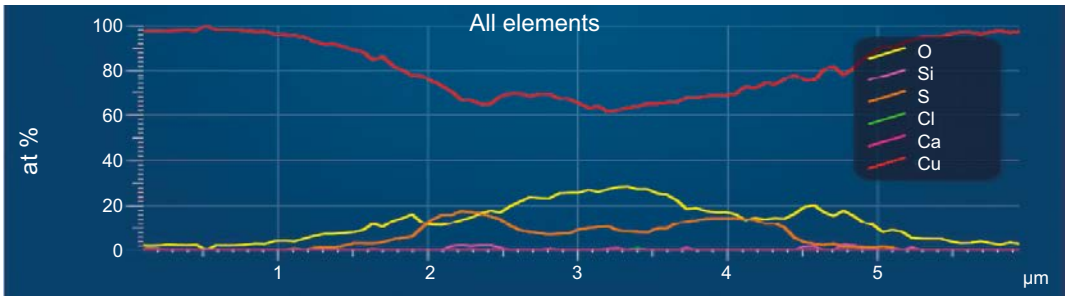

Figure 3-26. *Element analyses along the Line Data 1 in Figure 3-25. (Run #3, 2 mM sulfide, 10 mM chloride, 90 °C).*

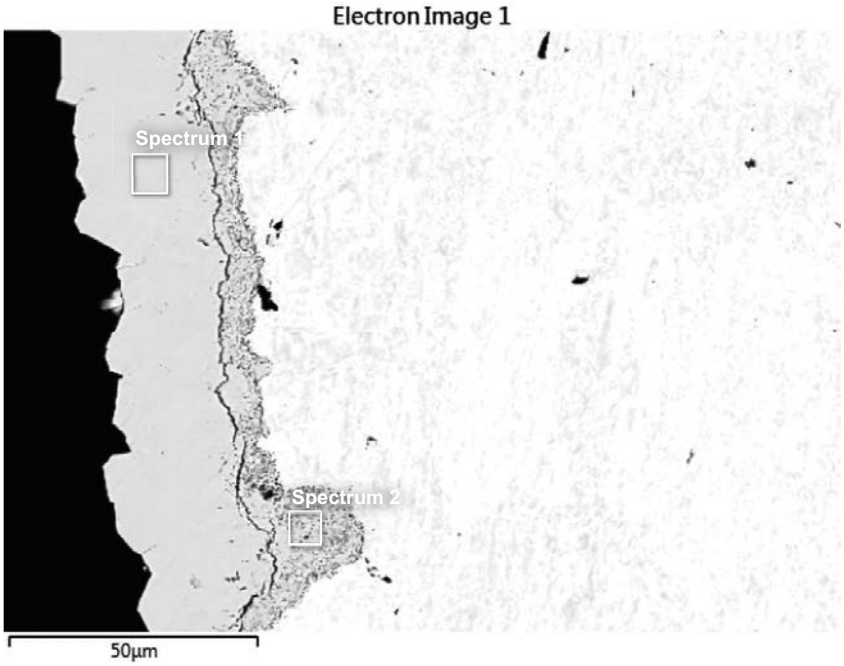

Spectrum Label	C	O	Si	S	Cl	Cu	Tot
Spectrum 1	3.65	0.42	0.09	29.04	0	66.8	100
Spectrum 2	5.11	4.11	0.23	25.96	0	64.59	100

Figure 3-27. *An image of the polished longitudinal cross section of the test rod from Run #4. The element analyses (in at %) are also shown (Run #4, 1 mM sulfide, 100 mM chloride, 90 °C).*

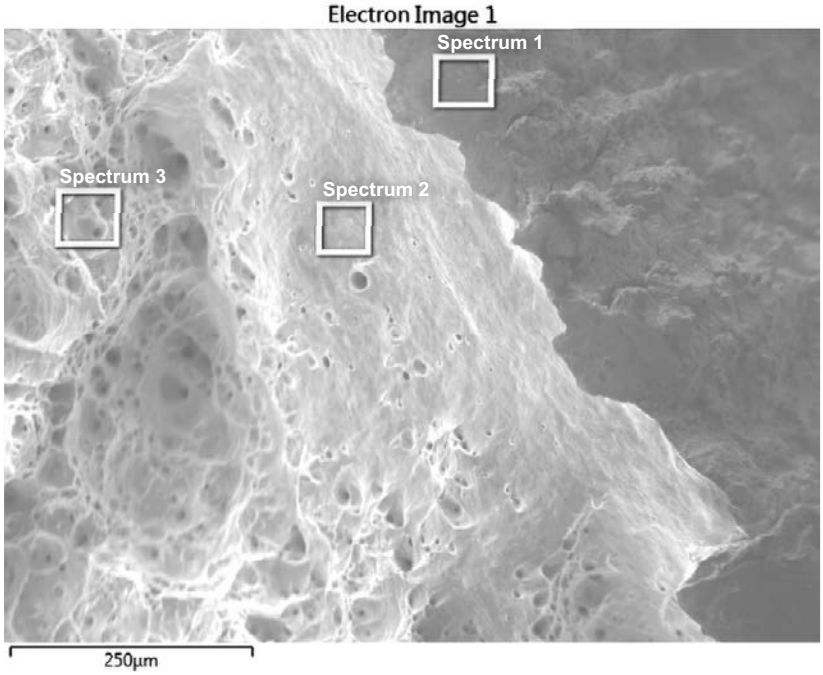

Spectrum Label	C	O	Si	S	Ca	Cu	Tot
Spectrum 1	0	1.39	0.64	11.21	0.18	86.58	100
Spectrum 2	0	0	0.82	8.19	0.17	90.82	100
Spectrum 3	0	0	0	2.61	0	97.39	100

Figure 3-28. *SEM image of the test rod from Run #5, 1 mM sulfide, 10 mM chloride, 60 °C. The fracture zone is seen to the left and the outer surface to the right. The locations for three areas of analyses are shown. The element analyses (in at %) are also shown.*

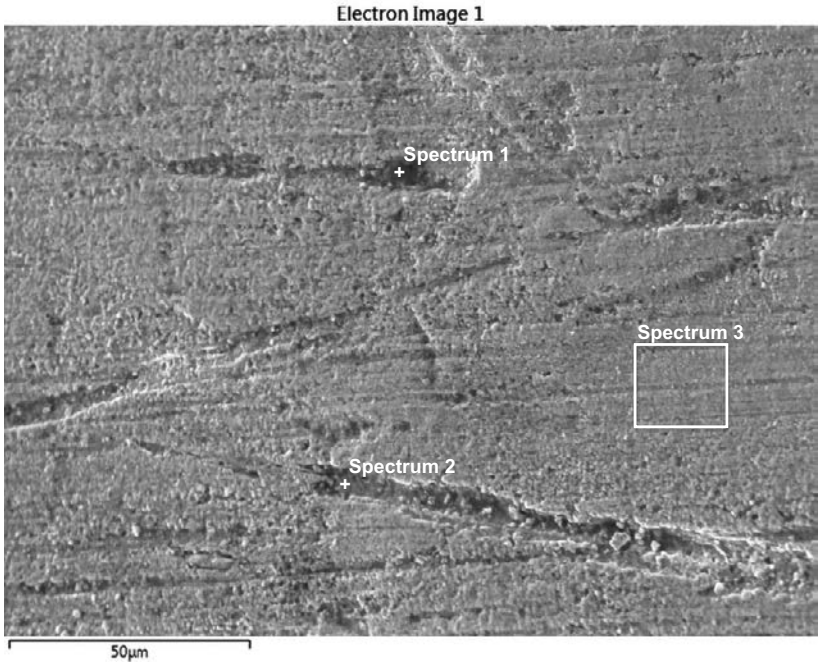

Spectrum Label	C	O	Si	S	Cl	Ca	Cu	Tot
Spectrum 1	64.59	9.56	8.69	6.54	0.03	1.43	9.15	100
Spectrum 2	17.55	19.31	16.88	14.23	0	0	32.03	100
Spectrum 3	13.08	5.62	4.07	26.54	0	0	50.69	100

Figure 3-29. *Image of the central part of the test rod from Run #6, 1 mM sulfide, 10 mM chloride, 60 °C, 2 days. The locations for three areas of analyses are shown. The element analyses (in at %) are also shown.*

Run #7, 1 mM sulfide, 10 mM chloride, 60 °C, 4 days

Figure 3-30 shows an image of the polished longitudinal cross section of the test rod from Run #7 with element analyses for three sites.

The site for Spectrum 24 is probably a sulfide inclusion. The low analysis result for sulfur is most likely caused by an analysis area that is much larger than the inclusion. Spectrum 25 probably also underestimates the local sulfide concentration. However, the source for the sulfur found in Spectrum 25 may be the solution. Slip lines, visible as a lighter color, can be seen in the grain to the left of the analysis points.

Run #8, 0.02 mM sulfide, 10 mM chloride, 60 °C

Figure 3-31 shows an image of the polished longitudinal cross section of the test rod from Run #8, 0.02 mM sulfide, 10 mM chloride, 60 °C. The locations for two areas of analysis are indicated. The element analyses are also shown. Sulfur is found at significant concentrations at both sites of analysis. Cu_2S is a likely constituent of the corrosion products also at this low concentration of sulfide. The appearance of calcium in Spectrum 1 indicates that this site may be a groove from the manufacturing where salt from the annealing melt has survived grinding and polishing.

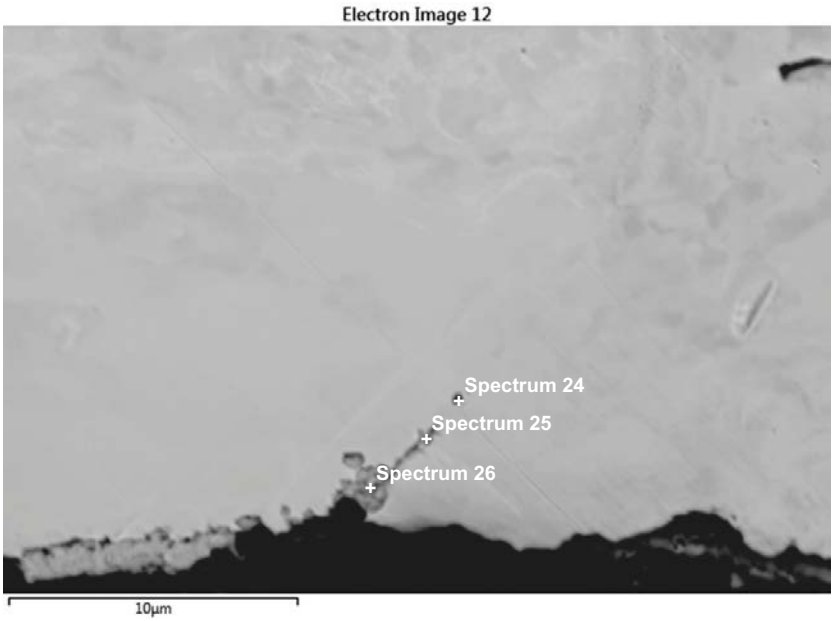

Spectrum Label	O	Si	S	Cl	Ca	Cu	Tot
Spectrum 24	2.2	0.25	0.07	0.09	0.06	97.33	100
Spectrum 25	7.14	0.77	1.61	0.12	0.03	90.33	100
Spectrum 26	11.38	1.04	20.47	0.31	0.08	66.72	100

Figure 3-30. *Image of the polished longitudinal cross section of the test rod from Run #7, 1 mM sulfide, 10 mM chloride, 60 °C, 4 days. The locations for three areas of analyses are shown. The element analyses (in at %) are also shown.*

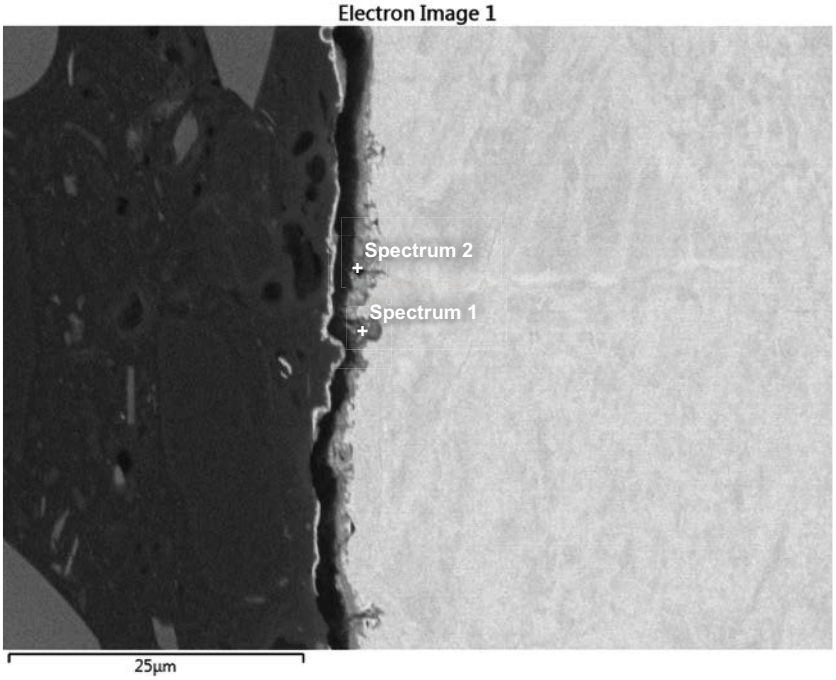

Spectrum Label	O	P	S	Cl	Ca	Cu	Tot
Spectrum 1	8.21	0	28.61	0	2.49	60.69	100
Spectrum 2	12.35	0	13.61	0	0	74.05	100

Figure 3-31. *Image of the polished longitudinal cross section of the test rod from Run #8, 0.02 mM sulfide, 10 mM chloride, 60 °C. The locations for two areas of analysis are indicated. The element analyses (in at %) are also shown.*

3.7 Grain size

The grain size of the material in the test rods was studied after electrolytic polishing to reveal the crystal shapes. The procedure followed was:

1. Mechanical polishing using diamond paste and silicon oxide.
2. Electrolytic polishing in 50 % ortho-phosphoric acid for 1 minute at 1.8 V and for 1 minute at 0.8 V relative to a copper plate.
3. Photographs taken by optical microscopy using polarized light.

Figure 3-32 shows a collection of images from the light optical microscopy of the test rods tested at 60 °C, Runs #5, #6 and #7 and the unexposed test rod. The images are taken from an area outside the necking region and few or no signs of grain deformation are visible in the images.

As the images in Figure 3-32 show, the grains are highly irregular in shape. Counting the number of grain boundaries from left to right in the image of the unexposed test rod, we end up with values between 17 and 21. The image spans a distance of 704 µm, from left to right. Divided by the number of grains, say 20, a measure of the average grain size is about 35 µm.

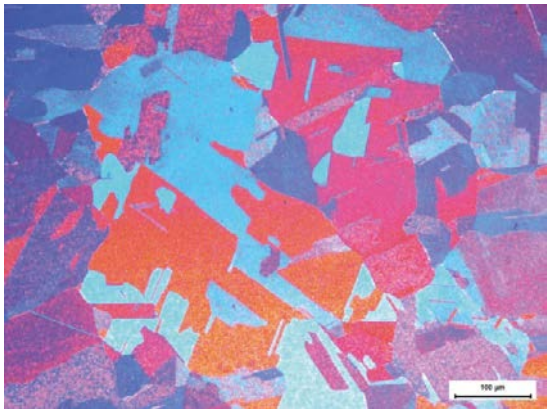

Test rod from Run #5

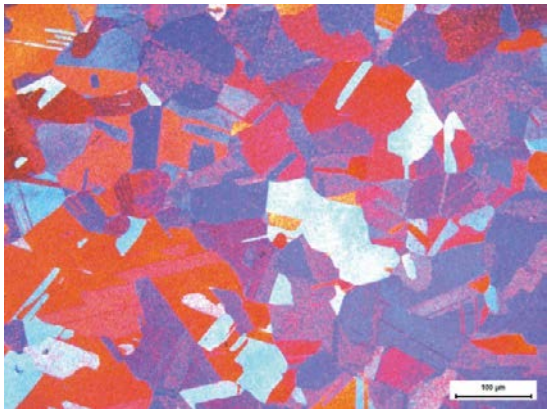

Test rod from Run #6

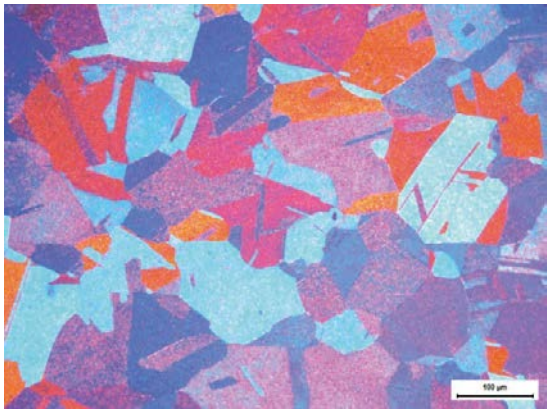

Test rod from Run #7

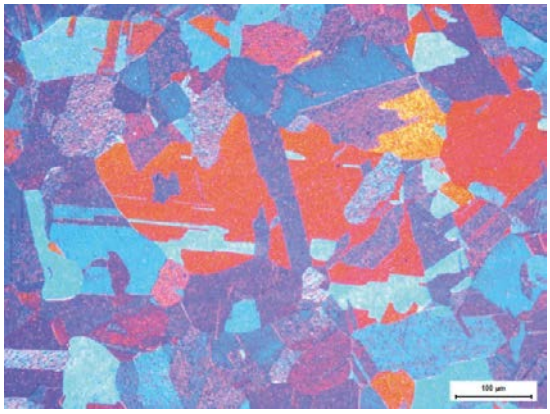

Unexposed test rod

Figure 3-32. *Light optical microscopy images of polished longitudinal cross sections of the test rods from Runs #5, #6 and #7 and one unexposed test rod.*

4 Discussion

4.1 Comments on the experimental results

4.1.1 Comment on the element analyses

The presence of carbon, calcium and silicon is indicated in several analyses. These elements are probably impurities from the manufacturing process. Calcium most likely comes from the salt melt used to anneal the test rods after machining. The origin of carbon could be lubricant used during the cutting action in the manufacturing process possibly converted to elemental carbon during the annealing. Carbon was also used together with silicon as SiC in the final polish of the test rods.

4.1.2 The distribution of cracks along the test rod

Figures 3-12 from Run #6 and 3-15 from Run #7 show that the first cracks appear towards the ends of the gauge section of the test rod. Figure 3-6 from Run #1 shows that the distribution is much more even at final rupture. We don't know the cause of the increased crack density towards the ends of the gauge section. Cracks at the ends of the gauge section apparently form faster than cracks located in the middle section. Some possible explanations are:

- Stress concentration at sites where the dimensions change. The stress may not be quite evenly distributed through the cross section close to where the diameter of the rod increases. The stress at the surface is likely to be higher towards the ends of the narrow section than in the middle.
- Galvanic effect between the narrow gauge section and the thicker ends of the test rods, Figure 2-2. The narrow section becomes more deformed during SSRT than the thicker ends. The narrow section may, because of the deformation, become anodic towards the rest of the test rod. Corrosion would occur preferentially at sites closer to the cathodic sites, i.e. at the ends of the gauge section. Cold work has been found not to give any measurable decrease in nobility of copper (Taxén et al. 2017). During strain, new copper surface is created and this may cause a temporary decrease in nobility.
- Galvanic effects between traces of carbon, at the ends of the gauge section, and bare metal. The dark circular patches close to the transition radius in Figures 3-18 and 3-19 may contain a residue of carbon. Figure 3-29 shows that carbon rich areas exist also at the central part of the test rod after Run #6. More elemental carbon at the ends of the gauge section would cause neighboring anodic sites to be more active because of the short distance to cathodic elemental carbon. The origin of elemental carbon could be lubricant used during the cutting action in the manufacturing process, converted to elemental carbon in the annealing. After polishing, such carbon would remain preferentially in the deep groves found mainly at the ends of the gauge section. Carbon films were once a problem for copper tubes, causing pitting corrosion. Lubricants used in the drawing of copper tubes degraded into elemental carbon films at the copper surface during heat treatment. The carbon films behaved as efficient cathodes and increased the corrosion potential to a level where pitting corrosion could occur (Mattsson 1980).
- Thermal effects. The test rod is heated only by the solution. At the ends, there are threaded connections to the machine. There are thermal insulators but there may still be a cooling action from the ends of the test rod. The present study revealed slightly more cracks at 60 °C than at 90 °C. An observation of more cracks towards cooler ends of the test rod than at the warmer middle of the rod would be consistent with this theory.
- Differences in surface finish. Figures 3-18 and 3-19 from the examination of an unexposed test rod show that there are remaining traces of the manufacturing process. Final finish was made manually using 600 grit paper and it is possible that the surface finish was more even at the middle of the test rod than towards the ends of the gauge section.

Becker and Öijerholm (2017) found numerous cracks also far from the narrowest part of their tapered test rod. These are presented in some detail in their appendix H that refers to their experiment #3 with a target sulfide concentration of 0.1 mM. None of the cracks from their experiment #3 were 'positively identified' as signs of SCC (Becker and Öijerholm 2017). No histogram over the locations of cracks is given but only examples of how such diagrams could be constructed.

4.2 Summary of observations from the present study

- Stress-strain curves show no significant dependence on the solution composition. (Figure 3-1)
- Intergranular cracks or intercrystalline corrosion was observed after the test in solution with 1 mM sulfide and 10 mM chloride at 90 °C. (Run #1, Figure 3-5)
- No such cracks were observed at after the test in solution with 0.02 mM sulfide and 10 mM chloride at 90 °C. (Run #2, Figure 3-5)
- More cracks were observed after test at 60 °C than at 90 °C. (Run #5 and Run #1, respectively)
- Fewer cracks were observed, at 90 °C, when the chloride concentration was increased from 10 mM to 100 mM. (Run #4 and Run #1, respectively)
- The initial cracks are preferentially located at the ends of the gauge sections of the test rods. (Figures 3-12 and 3-15)
- Tests at 60 ° interrupted after two or four days of testing show maximum depths similar to maximum (secondary) crack depths at rupture, after approximately 14 days. (Runs #6 and #7)
- Necking and final rupture occurs close to the middle of the gauge section. (Figure 3-9)
- Solid corrosion product, presumably Cu_2S, is frequently seen as detached particles rather than as thin films on the surface. (e.g. Figure 3-8)

4.3 Limitation of the low sulfide reference experiments

No crack like features were observed after Runs #2 and #8 in 0.02 mM sulfide. But an influence of oxygen was deduced from the measured corrosion potentials for these experiments. The element analysis in Figure 3-24 shows a significant concentration of phosphate in the corrosion products at the outer surface of test rod from Run #2. Phosphate is sometimes used as a corrosion inhibitor for copper in tap water systems (Schock et al. 1995). An inhibiting compound at a phosphate level of 3 mg/L may be $Cu_3(PO_4)_2$ but other modes of inhibition by phosphate are not excluded (Dartmann et al. 2010). Because of the inhibiting properties of phosphate on the corrosion of copper, the absence of crack-like features does not mean that 0.02 mM sulfide is a safe level and that such crack-like features cannot form at this sulfide concentration. In the present experiments at 0.02 mM sulfide there was the additional effect of oxygen ingress and formation of Cu(II), which is a constituent in $Cu_3(PO_4)_2$.

4.4 Theoretical background

It may be useful to discuss the probable main reactions during corrosion of copper in sulfide containing waters during hydrogen evolution.

4.4.1 Chemical reactions during corrosion

The overall corrosion reaction, in near neutral solution, with $Cu_2S(s)$ and H_2 as products can be written:

$$2\,Cu(s) + HS^- + H_2O \rightarrow Cu_2S(s) + H_2 + \ OH^- \qquad (4\text{-}1)$$

The anodic reaction to $Cu_2S(s)$ can be written:

$$2\,Cu(s) + HS^- + OH^- \rightarrow Cu_2S(s) + 2e^- + H_2O \qquad (4\text{-}2)$$

The anodic reaction to dissolved copper sulfide species can be written:

$$Cu(s) + HS^- \rightarrow CuHS(aq) + e^- \qquad (4\text{-}3)$$

$$Cu(s) + 2HS^- \rightarrow Cu(HS)_2^- + e^- \qquad (4\text{-}4)$$

Precipitation reactions of dissolved copper sulfide species can be written:

$$2CuHS(aq) + OH^- \rightarrow Cu_2S(s) + HS^- + H_2O \quad (4\text{-}5)$$

$$2Cu(HS)_2^- + OH^- \rightarrow Cu_2S(s) + 3HS^- + H_2O \quad (4\text{-}6)$$

The cathodic hydrogen evolution reaction, from water, can be written:

$$2H_2O + 2e^- \rightarrow H_2 + 2OH^- \quad (4\text{-}7)$$

In sulfide solutions, the HS^- ion could conceivably also participate in the cathodic reaction:

$$HS^- + e^- \longrightarrow S^{2-} + ½H_2 \quad (4\text{-}8)$$

Because of the instability of the S^{2-}-ion, a rapid reaction with water would follow:

$$S^{2-} + H_2O \longrightarrow HS^- + OH^- \quad (4\text{-}9)$$

4.4.2 Stability diagrams and solubility

The test solution contains chloride as well as sulfide. It may be useful for the interpretation of the results to study some stability diagrams for solid and dissolved species.

Several points will be emphasised:

- How supersaturated solutions arise.
- The effect of pH on the concentration of dissolved copper.
- The strength of the dissolved sulfide complex species with copper relative to the corresponding chloride complexes.

Figures 4-1 and 4-2 show stability diagrams for copper in 1 mM sulfide with 100 mM chloride at 25 and 90 °C, respectively. The diagrams were calculated from thermodynamic data in Puigdomenech and Taxén (2000). But complex constants for $Cu(HS)_2^-$ and CuHS(aq) were taken from Mountain and Seward (1999, 2003) with the temperature dependences reported there. Table 4-1 shows the stability constants that the diagrams are based on.

Table 4-1. Stability constants for dominating aqueous sulfide (HS^-) and chloride complexes at 25 and 90 °C, respectively.

	lg k(25 °C)	lg k(90 °C)
$Cu(HS)_2^-$	17.3	15.0
CuHS(aq)	13.0	11.4
$Cu_2S(HS)_2^{2-}$	29.3	22.0
CuCl(aq)	3.3	3.3
$CuCl_2^-$	5.6	5.2
$CuCl_3^{2-}$	4.9	4.4

The solid black line shows the maximum potential that can arise at hydrogen pressure of 1.0 atm if there are no oxidants other than water. The 1.0 atm pressure and the location of the black line are not absolute limits for the potentials that hydrogen evolution can generate but it is a useful reference limit. At lower levels of dissolved H_2 slightly higher potentials can arise. The dashed black line corresponds to a partial pressure of 0.1 atm H_2. The thick red line shows the boundary between the stability domains of copper metal, Cu(s) and copper sulfide, $Cu_2S(s)$. The thin red curve and the dashed red curves show equilibrium potentials for the dissolved species $Cu(HS)_2^-$, CuHS(aq) and $Cu_2S(HS)_2^{2-}$, respectively at concentrations of 1.0 µM. These concentrations are not in equilibrium with the solid $Cu_2S(s)$ nor with one another. If they were, the lines would coincide with the line for Cu(s)/Cu_2S(s).

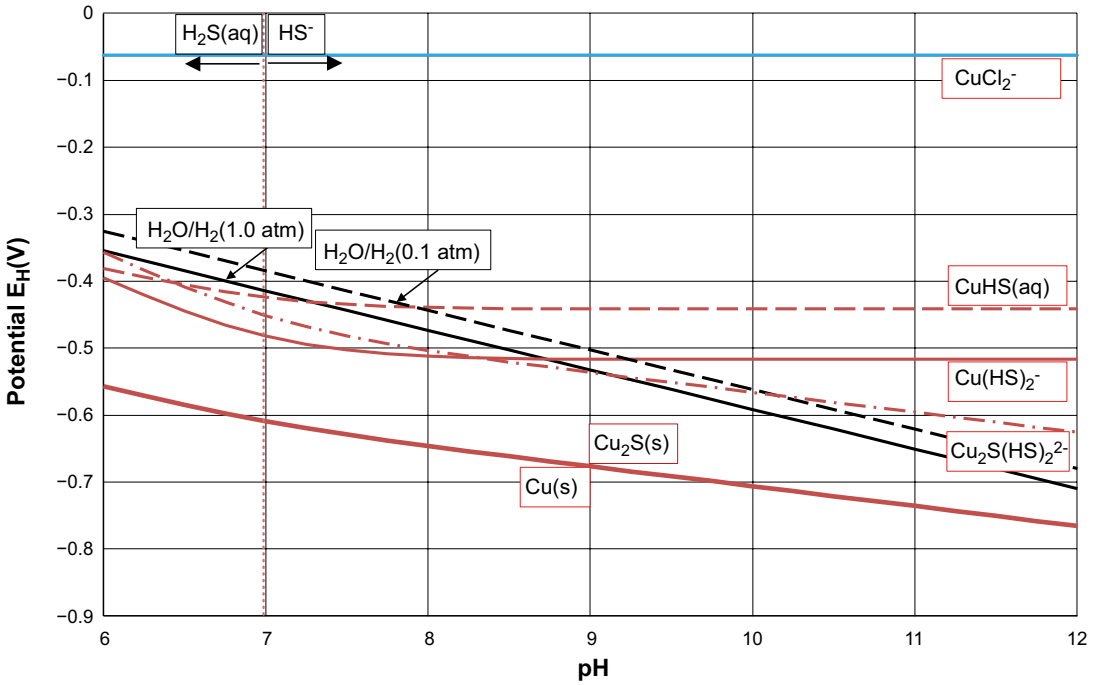

Figure 4-1. *Stability diagram for copper in 1 mM sulfide and 100 mM chloride at 25 °C. The dissolved copper containing species are shown at a concentration of 1 µM.*

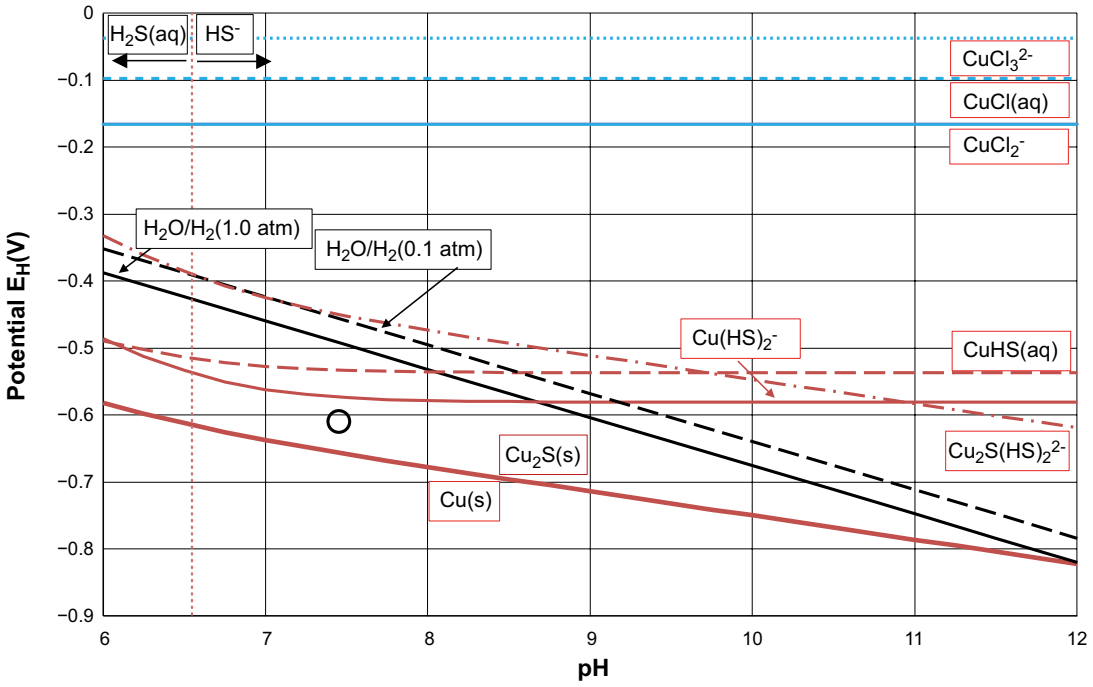

Figure 4-2. *Stability diagram for copper in 1 mM sulfide and 100 mM chloride at 90 °C. The dissolved copper containing species are shown at a concentration of 1 µM. The black circle at pH 7.4 represents the results from the present work at 90 °C.*

4.4.3 Supersaturated solutions

The selected concentrations of $Cu(HS)_2^-$ and CuHS(aq) require higher potentials in order to form than the solid copper sulfide. The hypothetical solution with these concentrations would be super-saturated with respect to $Cu_2S(s)$.

If we focus on Figure 4-2, for 90 °C, the curves for the dissolved copper sulfides require higher potentials to form at the selected concentration than hydrogen evolution to 1.0 atm can give at high pH. But at values below pH 8, hydrogen evolving corrosion can create the selected concentration. It would not be the lowest energy state, which would be equilibrium with $Cu_2S(s)$, but it would be a downhill process. However, if the solid $Cu_2S(s)$ was formed first, dissolution cannot generate concentrations of the selected level of 1.0 µM. That would be an uphill process.

The black circle at pH 7.4 represents the results from the present work at 90 °C. The corrosion potential, about –0.608 V, E_H (–0.850 V vs SCE + 0.242 V) is located below all the lines for dissolved concentrations of 1.0 µM. The potential is not sufficiently high to generate these concentrations by corrosion of copper with its usual properties. However, if copper at grain boundaries, under stress and strain behave as slightly less noble, corrosion of these less noble grain boundaries could generate concentrations of dissolved copper that would make copper in grain bodies, copper with its usual properties, behave as immune.

4.4.4 The effect of pH on the concentrations of dissolved copper

In the present experiments at about pH 7.2–7.4, dissolved concentrations slightly lower than 1.0 µM can arise from corrosion of copper with its usual properties. The measured corrosion potential is well below the solid black line for hydrogen evolution at 1.0 atm, leaving a significant margin for activation potential to actually generate hydrogen. But at pH 12 the solid black line intersects the solid red line, representing the stability limit for $Cu(s)/Cu_2S(s)$ in Figure 4-2. While $Cu(s)/Cu_2S(s)$ may coexist with H_2 at 1.0 atm, there would be no or very small margin for the necessary activation potential to actually generate hydrogen. At potentials significantly higher than the intersection point at pH 12, only small amounts of hydrogen can form until local equilibrium limits the production. At potentials significantly lower than the intersection point at pH 12, only very small amounts of dissolved copper sulfide can form and no $Cu_2S(s)$. The potential at the intersection point seems to be a reasonable prediction of the corrosion potential in 1 mM sulfide at pH 12 and 90 °C. As Figure 4-2 shows, the complex species $Cu_2S(HS)_2^{2-}$ is the most stable form of dissolved copper at pH 12. The predicted corrosion potential is about 200 mV lower than the equilibrium potential for a 1.0 µM concentration of $Cu_2S(HS)_2^{2-}$.

In conclusion, very low concentrations of dissolved copper are likely to form at high pH. The decrease in oxidising property of water at high pH is a main factor. Another, unrelated, factor is the decreasing solubility of $Cu_2S(s)$ with increasing pH.

4.4.5 Chloride complexes relative to sulfide complexes

At relatively high potentials there are one or three lines in blue. These lines represent the potentials required to form the dissolved copper chloride complexes CuCl(aq), $CuCl_2^-$ and $CuCl_3^{2-}$ at concentrations of 1.0 µM. The lines are located at potentials much higher than the black line. The lines for CuCl(aq) and $CuCl_3^{2-}$ are located at a potential higher than 0 V at 25 °C and falls outside the scale in Figure 4-1. Hydrogen evolution to 1.0 atm cannot produce concentrations of 1.0 µM for any of the chloride species, at the chloride concentration of 0.1 M.

Figure 4-3 illustrates the relative stability of the sulfide and chloride complexes with copper. The figure shows distribution diagrams for dissolved copper in 0.1 M chloride as function of sulfide ion concentration. The diagrams are drawn for pH 7.5 and solubility equilibrium with $Cu_2S(s)$.

Figure 4-3 shows that the chloride complexes are very weak relative to the complexes with hydrogen sulfide. At sulfide concentrations as low as 10^{-6} M, virtually all dissolved copper would be present in the form of sulfide complexes. The exchange of ligands from sulfide to chloride can thus not be a significant step in the process. Under conditions where the chloride complexes may be of significance, the concentration of sulfide would have to be so low that the presence of sulfide could have no influence on the corrosion of copper.

While Figure 4-2 shows that copper chloride complexes cannot be significant primary corrosion products because the corrosion potential, at least at 90 °C, is too low, Figure 4-3 shows that a ligand exchange from sulfide to chloride can also not be significant.

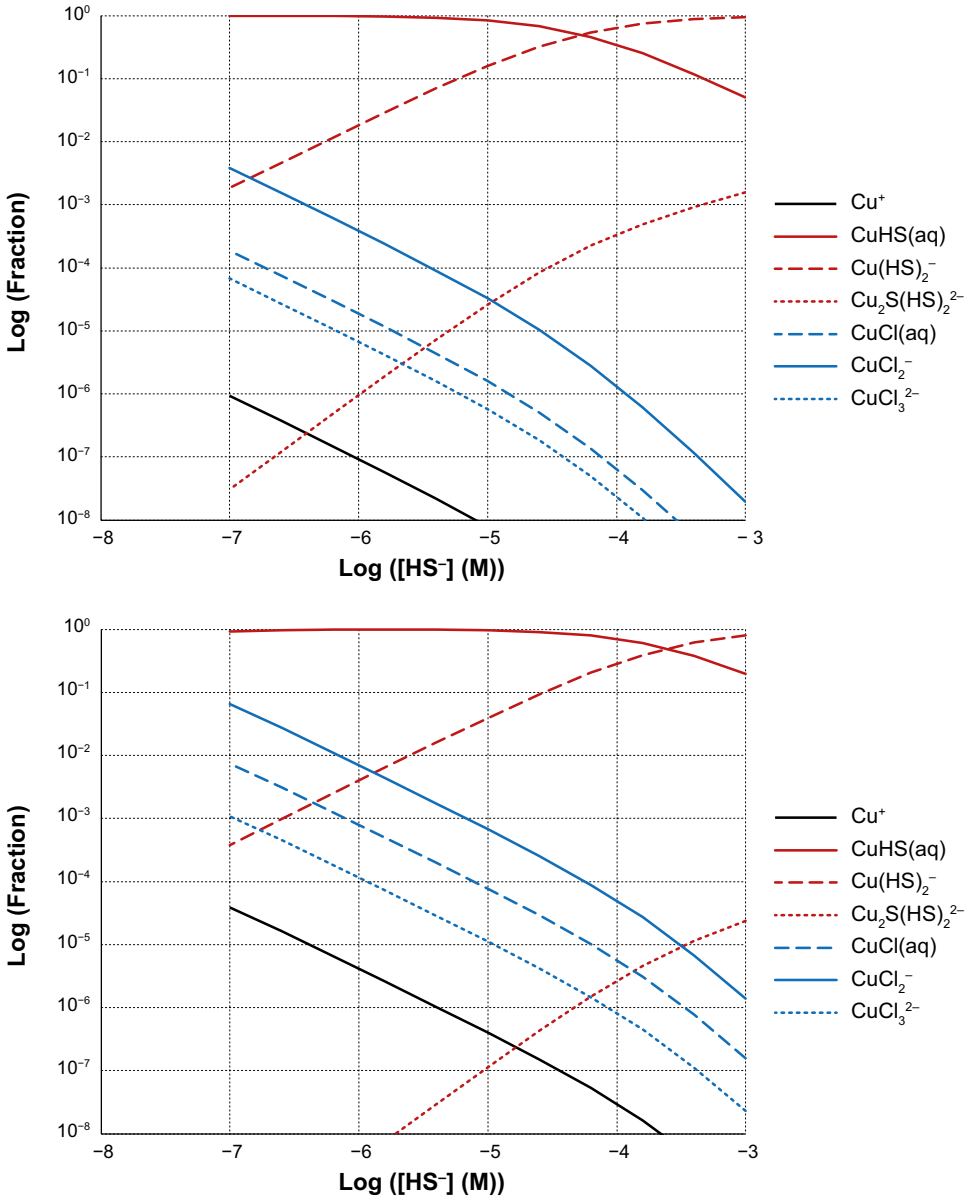

Figure 4-3. *Distribution diagrams for dissolved copper in 0.1 M chloride as function of sulfide ion concentration. 25 °C upper diagram and 90 °C lower diagram.*

4.5 Interpretation of results

Figure 4-4 illustrates a background for the interpretation of the SEM-observations of the crack-like surface features. For simplicity we will refer to them as cracks. The cracks are not visible in the tests at very low sulfide concentrations, so it is deduced that the action of sulfide at the deepest end of the crack is a prerequisite for propagation. Bare copper metal seems relatively reactive towards sulfide, so it is reasonable that the surface at *C* is at least partially protected by Cu_2S before a significant sulfide concentration can form at point *B*. Likewise, the copper surface at point *B* would have to be partially protected by Cu_2S before there is a significant transport to point *A*. We conclude that most of the copper will have to be covered by a, more or less, protective layer of copper sulfide before the crack can propagate.

Sulfide, in near neutral solutions, appears in two aqueous forms, hydrogen sulfide ion, HS^- and dihydrogen sulfide H_2S(aq). The latter neutral H_2S(aq) dominates below pH 7.0 and HS^- dominates at higher pH values. In the tested solutions with pH values between 7.2 and 7.5 only about 10 % of the total sulfide concentration is present as H_2S(aq).

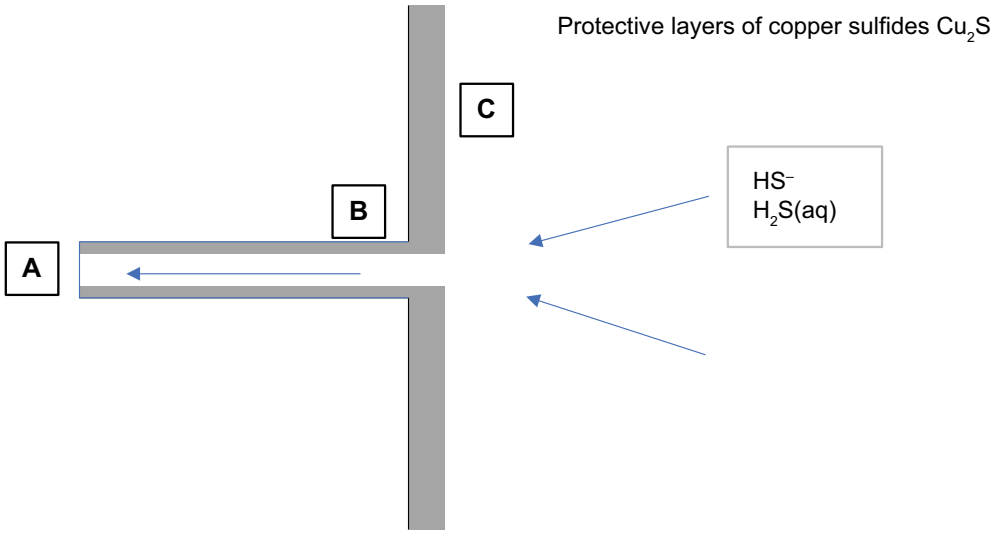

Figure 4-4. *Sketch of a propagating crack induced by sulfide from the solution.*

We will first give an overview of possible mechanisms for the observed features and then try to correlate observations with the various mechanisms.

4.6 Some possible mechanisms

Stress corrosion cracking of copper is discussed, in some detail, by King et al. (2010) and King and Newman (2010).

Among the mechanisms for stress corrosion cracking of pure metals we find:

- Slip dissolution
- Film fracture
- Vacancy injection
- Intergranular corrosion
- Hydrogen embrittlement

4.6.1 Slip dissolution

According to this model (Newman 2002), crack growth occurs by extremely localized anodic dissolution. The sides of the crack are protected by a film, usually an oxide, which is fractured as a result of plastic strain in the metal at the crack tip. Crack growth proceeds by a cyclic process of film rupture, dissolution, and film repair. The model implies that a crack will stop unless there is a slip that ruptures the protective film.

The film-rupture/anodic–dissolution model and Tarnish-rupture mechanism are similar to the slip dissolution model but the site of the crack is not necessarily connected to any slip bands in the metal.

4.6.2 Film fracture

In the context of pure copper and sulfide, the film fracture mechanism implies that a film of copper sulfide fractures under the tensile stress and that this fracture also affects the underlying copper metal. A prerequisite would seem to be a very strong adhesion between copper sulfide and copper.

4.6.3 Vacancy injection

This theory is described in general terms in Aaltonen et al. (1996) and applied to copper in Aaltonen et al. (2003, 2015), and reviewed in Huotilainen et al. (2018).

Vacancy injection implies that a surface copper atom that is oxidized is replaced by another copper atom from a deeper layer. Thus, a vacancy is formed in the metal. Repeated processes results in a weakening of the metal lattice. Under tensile stress and strain the vacancies can multiply and allow crack propagation from the site of the corrosion attack that generates the vacancies. The theory is applied specifically to transgranular SCC of copper. Only intergranular corrosion attacks were observed in the present study.

4.6.4 Surface mobility model

Galvele's surface mobility model, according to Newman (2002), proposes that cracks grow by surface diffusion of metal atoms (possibly combined with ions or molecules from the environment) from a very sharp crack tip to the crack walls, i.e., capture of vacancies by the crack tip.

4.6.5 Intergranular corrosion

Intergranular corrosion (IGC) or grain boundary corrosion of copper is discussed by King et al. (2010). The tendency for IGC of copper was studied by Fennel et al. (2001) and by Gubner et al. (2006) with emphasis on copper welds. However, none of these studies included sulfide.

Intergranular corrosion is strictly not a mechanism for stress corrosion cracking. IGC can probably initiate SCC by stress concentration (Newman 2002). But, tensile stress can probably also aggravate intergranular corrosion without transition to SCC. The access of sulfide to grain boundaries is facilitated if the grains are pulled apart by tensile stress. IGC may be initiated by accumulation of impurities and doping elements.

Grain boundary segregation of nonmetallic impurities influences many chemical and mechanical properties (Oudar 2002). It increases the metal brittleness, favors hydrogen embrittlement, decreases the intergranular fatigue strength or the creep rupture life, and favors IGC and SCC. In this respect, sulfur is one of the most detrimental elements (Oudar 2002), at least in nickel or iron-based alloys.

Figure 3-25 shows an intergranular attack that appears to have propagated through some kind of inclusion or impurity. The element analysis gives no indication as to the nature of the inclusion or impurity.

Miyamoto et al. (2007) explain the intergranular corrosion of copper without impurities: "In heterogeneous structures, the defects, such as dislocations and grain boundaries, have an excess free energy. Therefore, their half-cell electrode potential is relatively low, whereas the grain bodies with a relatively low energy have the higher half-cell electrode potential. Thus, there is a spatial distribution of the potential along the surface. The degree of local corrosive attack leading to the heterogeneous corrosion is well associated with these two half-cell potentials and oxidizing power of the solution, which is given commonly by an equilibrium potential of reduction reaction. When the oxidizing power lies between the half-cell electrode potentials of grain boundaries and grain interior, the anodic cites are distributed along the grain boundaries, promoting the easier local attack at the grain boundaries. The large cathode area facilitates the reduction reaction so that the anodic dissolution current must increase to comply with local electric neutrality. In other words, when the area of grain interior is larger by orders of magnitude than that of grain boundaries, the penetration rate at the grain boundaries is enhanced."

Intergranular corrosion of copper is a well-known phenomenon. Al Kharafi et al. (2008) found intergranular corrosion of 99.9 % copper immersed for 24 h at the free corrosion potential in 3.5 % NaCl + 10^{-3} M HS^-. The process could be further promoted by applying an oxidizing potential.

The same group of researchers found intergranular corrosion of copper in the presence of benzotriazole (Aboubakr et al. 2006). They found that extensive intergranular corrosion occurred in the presence of 10^{-3} M BTAH with 3.5 wt% NaCl at a potential of 0.2 V (Ag/AgCl).

4.6.6 Hydrogen embrittlement

Yagodzinskyy et al. (2012) showed that surface cracks appeared in oxygen-free phosphorus-doped copper when electrochemically charged by hydrogen during mechanical stress by constant load. The cracks were intergranular and correlated with the appearance of hydrogen filled micro-voids. The authors conclude: "Hydrogen introduced electrochemically into oxygen-free phosphorus-doped copper

has a minor effect on the tensile SSRT properties of copper. The small reductions in uniform elongation and tensile strength in the tests with continuous hydrogen charging at 50 °C originate from the cracks forming in the hydrogen enriched subsurface layer."

In the absence of other oxidants in the system, hydrogen is formed from reduction of protons, from the cleavage of water or from reduction of the hydrogen ions that were bound to the reacting sulfide species. Hydrogen gas can, in principle, form but hydrogen molecules may also stay dissolved in the water. Intermediate adsorbed hydrogen atoms may diffuse into the metal and cause an embrittlement by interfering with metal-metal bonds, form water vapor together with impurities of oxygen or form hydrogen filled micro-voids (Yagodzinskyy et al. 2012).

4.7 Inhibiting processes

The sketch in Figure 4-4 seems to be applicable to all the mechanisms considered. Figure 4-4 emphasizes the necessity of transport of sulfide from the solution to the propagating front of the crack. For hydrogen embrittlement the transport of sulfide to the crack front may not strictly be necessary but if the corrosion takes place at other sites there does not seem to be any reason for the cathodic reaction to take place at the crack front. The crack front behaving as a net cathode seems highly unlikely. Some processes that would interfere with the sulfide transport are:

- Competition from other sites. The outer surface, *C*, as well as the crack walls, *B*, could decrease the flux of sulfide by corrosion at these sites.
- Blockage of the passage at *B* by solid corrosion products.
- Surface charge at point *B* that causes adsorption of HS^- if the surface charge is positive or exclusion of HS^- if the surface charge is negative. The adsorption of sulfide species could in turn be affected by competing sorption of other species, e.g. chloride ions or complexes.
- Particularly for very narrow sections of a propagating crack where the dimensions of the crack approaches molecular level, ions that require solvation water molecules and counter ions may be excluded for steric reasons. Thus HS^- may become excluded but $H_2S(aq)$ may reach the crack front.

At potentials where copper can corrode to significant concentrations of chloride complexes, e.g. $CuCl_2^-$, diffusional flux of oxidized copper from corrosion at points *A* and *B* towards the bulk solution would instead form sulfide complexes or precipitate as Cu_2S when the bulk sulfide concentration is encountered. Sulfide would thereby be consumed and at least partly be prevented from reaching point *A*. As indicated in Figures 4-1 and 4-2 potentials much higher than hydrogen evolution can generate in near neutral solutions, are required to form dissolved chloride complexes at significant concentrations.

4.8 The role of stress and strain in intergranular corrosion of copper

As discussed in Section 4.6.5, stress and strain can probably aggravate intergranular corrosion. Stress can possibly increase the free energy at a grain boundary thereby making the boundary more prone to corrode. Strain, pulling adjacent grains apart, can modify the geometry of an intergranular attack so that a wedge shaped cavity is formed rather than a rectangular or rounded cross section.

Let us consider the crack (IGC) attack in Figure 3-22 as an example. Assume that the feature is caused by IGC and that no cracking was involved in its formation. In the absence of any strain the distance between Grain 1 and Grain 2 would probably be much smaller and in the absence of any IGC, the grains would be more deformed. Because of the IGC-feature, the grains are less deformed and partly just translated in opposite directions by the strain. This translation of the grains leads to a widening at the mouth of the IGC-feature. The widening at the mouth would facilitate the aqueous mass transport of sulfide to the propagating front and of corrosion products from the propagating front of the IGC, and also decrease the solution resistance in an electric circuit where the cathode is located outside the cavity. Brittle protective layers at the front may crack by the strain and allow propagation of an intergranular attack, that is if protective layers are formed. Transition to SCC, with a slip dissolution mechanism, would take place if the protective layer at the front cracks by slips in a repeated step wise

propagation. Transition of IGC to SCC according to other mechanisms seems also possible. Returning to the crack-like feature in Figure 3-22, none of the other types of SCC-mechanisms discussed seem necessary in order to explain the appearance of the feature. On the other hand alternative mechanisms that result in intergranular crack like features cannot be excluded based on the shape of the crack like feature. The metallographic examinations in Section 3.5 show few places where there seems to be an adherent film that could crack, although the corrosion products may have been more adherent in the absence of stress and strain.

4.9 Films of corrosion products on copper in sulfide solutions

The corrosion products and their solubility and morphology are suggested to have an importance for the development of cracks. The morphology of films formed in sulfide solution was extensively studied at the University of Western Ontario.

Smith et al. (2007) studied the sulfide film formation on copper under electrochemical and natural corrosion conditions. They found that

- At a sulfide concentration of 10^{-3} mol/L, film growth can follow two distinct pathways. The initially formed film grows via the transport of Cu(I) ions (or an associated defect) through the sulfide film. If this film remains intact, then film growth is limited and a steady-state thickness is achieved. If the development of interfacial stresses leads to film fracture, then growth can continue and much thicker nodular deposits, confirmed using SEM, are formed.
- When an intact sulfide film is present the corrosion potential achieves a value very close to the equilibrium potential for the sulfide formation reaction. This, and the observation that the cathodic current for H_2O reduction is very small and potential independent, shows that the sulfide formation reaction is rate-determining.

The observations refer to room temperature, a pH estimated to about pH 11 and no applied stress.

In a later study, Smith et al. (2009) report on a study of the influence of chloride on the corrosion of copper in aqueous sulfide solutions. At the lowest chloride concentration studied, 0.1 mol/L solution, they found a thin layer of sulfide on the surface after only 1 h exposure at the open circuit potential. SEM micrographs showed the presence of a base layer with some porosity and, with time, an outer deposited layer formed which uniformly covers the electrode surface.

At higher chloride concentrations, a similar progression from an initially formed base layer to the deposition of an outer layer was also observed. The morphologies of the layers vary with Cl^- concentration. As the Cl^- concentration is increased, the rapidly formed base layer present after 1 h of exposure increases considerably in roughness and porosity and the outer deposited layer appears less well-formed and less uniform.

- Sulfide films were observed to grow initially as a thin base layer of $Cu_{1.8}S$ which developed porosity allowing the further growth of a much thicker outer deposited layer of Cu_2S.
- In 0.1 mol/L chloride solution, this outer layer was dense and compact and eventually sealed the pores in the base layer, a situation which would lead to low corrosion rates.
- When the chloride concentration was increased to 1.0 mol/L, the base layer became more porous and the outer layer less dense and less compact, and the pores in the base layer were not sealed.

Chen et al. (2017) studied micro galvanic effects on copper related to non-uniform film growth in aqueous sulfide solutions containing chloride. At a junction between a surface exposed for 1691 h and an area exposed to 480 h (wax covered for the first 1211 h) the corrosion attack is amplified. Deeper, open cavities are formed under the thicker layer of corrosion products. Apparently the thicker and more crystalline layers behave as more efficient cathodes and corrosion is amplified by the presence of and proximity to large crystals. Also when a precorroded specimen with relatively large crystals of corrosion products is separated but electrically connected to a fresh copper surface the fresh copper surface corrodes faster than it would without the electrical connection. The crystals at the cathodic, precorroded surface were found to grow faster because of the coupling to fresh surface. Apparently, there is a transport of dissolved copper from anodic sites to cathodic sites. This aspect was later studied

in some detail (Chen et al. 2018). The galvanic current increased with time and with increased size of crystalline corrosion products at the cathode. Solution analysis verified the presence of significant amounts of dissolved copper (Chen et al. 2017).

It seems possible that precipitation and crystal growth could be stimulated by a higher pH at the cathodic sites (caused by the cathodic reaction). The precipitation of both $Cu(HS)_2^-$ and CuHS(aq) may have OH^- as a reactant (Reactions 4-5 and 4-6).

Conversely, the precipitation reactions prevent the alkalization at the cathodic Cu_2S crystals and thereby serve to maintain the driving force for corrosion.

The authors conclude (Chen et al. 2017):

"Non-uniform growth of the corrosion products on Cu in aqueous SH^- solutions results in a potential difference between the 'thick' and 'thin' films. Such a potential difference, though small, leads to variations in corrosion rate since Cu corrosion in aqueous SH^- solutions require very little overpotential. When this occurs some locations accumulate thick partially protective corrosion films at which the corrosion rate is low while others become covered only with non-protective thin and porous deposits and experience a higher corrosion rate. This leads to the establishment of microgalvanic couples with areas protected by corrosion product deposits acting as cathodes and unprotected areas as anodes. To sustain these couples Cu transport via surface and/or solution transport processes from anodic locations to cathodic locations must occur."

Thus the work of Chen et al. (2017) emphasizes the electrochemical nature of sulfide corrosion of copper and suggests that corrosion products are not only a result of corrosion but that the presence of crystalline corrosion products in metallic contact with copper can be a cause of the corrosion, locally.

4.10 Crack shape and amount of corrosion products

Cracks formed predominantly from mechanical separation between neighboring grains would be expected to be wedge shaped and narrow. Directions roughly perpendicular or at 45° angle to the surface would be preferred. No particular accumulation of solid corrosion products is expected.

Cracks formed predominantly from intergranular corrosion could be wide or they could be narrow. Wedge shapes could arise by continuous strain after the crack was formed. No particular orientation of crack growth is predicted but cracks perpendicular to the stress and strain would grow wider at the mouth which could facilitate mass transport to the front of the crack. The sites of cracks formed predominantly from intergranular corrosion would be expected to be associated with more solid corrosion products than sites far from any crack.

Runs #1, #4 and #5 all produce relatively sharp cracks, Run # 3 produces wider cracks with more rounded shapes. Figure 3-7 shows representative examples of the latter.

The cracks in Run #1 generally contain solid corrosion products that do not fill the cavity. The corrosion products generally do not follow the contours of the crack walls. The impression is that the cracks are opened more by the movement of neighboring grains than by corrosion.

The solid corrosion products in Run #3 seem more voluminous and seem to follow the crack profile and frequently fill the entire crack volume. Run #4 shows a concentration of cracks at the ends of the gauge length. These cracks are generally wide and have a comparatively large radius at the front. The similarity between these cracks and features found at the unexposed test rod suggests that these wide cracks may have been present before exposure and testing. However, there are also fine cracks where intergranular corrosion has occurred some distance into the material. The lower images in Figure 3-8 show an example where there is a lack of directionality that is not readily connected to any mechanical stress or strain. There are no solid corrosion products visible in the deeper part of the cavity but only half way out of the crack and outside. The impression is that copper has corroded to a dissolved form and precipitated at another site. This is consistent with CuHS(aq) and $Cu(HS)_2^-$ being primary corrosion products and Cu_2S being precipitated where the alkalizing effect from the cathodic reaction is encountered. The intergranular nature of the corrosion could be explained by the near equilibrium conditions. Small differences in stability between grain boundary and grain interior may be the cause.

The site of the cathodic reaction would probably be relatively close to the sites for anodic dissolution, as large distances in the narrow geometry would give high iR drops. There are no apparent large crystals of corrosion products that would serve as cathodic sites in Figure 3-8. The corrosion mechanism suggested by Chen et al. (2017) implies large, and growing, crystals of corrosion products in metallic contact with the copper metal. Figure 3-10 shows sites where the proximity between cracks and large grains of corrosion product could suggest a causal relation. But there are many such grains that are not associated with cracks. A difference between the conditions for Figure 3-8 and Figure 3-10 is that the conductivity of the solution is lower in the latter experiment so that galvanic effects have a shorter range. The temperature is also lower for Figure 3-10 than for Figure 3-8.

Figure 3-8 does not show any tendency for solid corrosion products to occlude the site of corrosion. Large amounts of corrosion products are formed outside the mouth of the crack but seem to be quite porous. The relatively even distribution of corrosion products over the surface suggests that even, general corrosion has been the dominating mode of corrosion and that oxidized copper from the intergranular corrosion constitutes only a small fraction of the solids deposited outside the site of the intergranular attack.

4.11 The role of chloride

As found in the theoretical background, the role of chloride in corrosion of copper in sulfide solutions is not to be found in the complex forming capacities of the chloride ion. This conclusion was reached also by Chen et al. (2018) for similar reasons.

However, chloride ions may still play a role in the corrosion process by contributing to and sometimes dominating the electrical conductivity of the solutions so that electrochemical corrosion with separate anodic and cathodic sites is facilitated. Increased chloride concentrations support higher cathode to anode area ratios. At the same time, the influence of a particularly efficient cathodic site (a large grain of Cu_2S crystal or a spot of elemental carbon) may be smaller in solutions with higher chloride concentration. The effect tends to be more spread out over a larger corroding surface and less local when the conductivity of the solution is higher. Higher conductivity supports higher anode/cathode area ratios but also higher cathode/anode area ratios.

Adsorption of chloride ion may have an influence. Chen et al. (2014) found that porous films of Cu_2S form when the concentration ratio chloride/sulfide exceeds 1000 and compact films form at lower ratios. A possible explanation is delayed crystal growth by adsorbed chloride ion at growing sites of Cu_2S grains. Consequences of delayed crystal growth and amorphous or porous Cu_2S would be higher degree of supersaturation and higher solubility.

4.12 The role of pH

Figure 4-5 summarizes the experimental result from previous work on SSRT testing of SKB-copper. The upper diagram illustrates the data points studied at room temperature and the lower diagram illustrates data points studied at higher temperatures. Open symbols are used to show that no signs that were interpreted by the authors as indications of SCC were found. Symbols filled with red indicate that signs indicating SSC were found.

Signs of SCC/IGC were found also at 100 mM NaCl in the present work and 2 mM sulfide was studied only at 90 °C. The work of Taniguchi and Kawasaki (2008) was not included in Figure 4-5. They studied copper of a different origin and found signs of SCC at conditions corresponding to those studied by Taxén et al. (2018) and by Bhaskaran et al. (2013) at 80 °C.

The diagrams represent the experimental conditions only in terms of two levels of temperature and scales for pH and sulfide concentration. The composition of the background electrolytes has also varied between the studies. All researchers added sulfide in the form of Na_2S to the test solutions. The natural pH of these solutions tends to be high. Bhaskaran et al. partly neutralized the solution in some experiments at room temperature. Becker and Öijerholm added a phosphate buffer to about pH 7.2. This procedure was copied in the present work. The base electrolyte otherwise varied between 10 mM NaCl, 100 mM NaCl and synthetic sea water (SSW) with a chloride concentration

corresponding to approximately 500 mM NaCl. Another variable, not visualized in Figure 4-5 is the strain rate. Signs that may be interpreted as SCC were found only in studies with low strain rate. This would suggest that the time of the exposure under strain may be of importance for the development of SCC. However, Runs #6 and #7, in the present work, were interrupted after 2 and 4 days, respectively. Signs of SCC/IGC were still detected by SEM after the shorter durations. Only the number of such signs, in the form of cracks or crack-like features increased with duration of the test. The maximum depth of the cracks increased only slightly with increasing duration of the exposures.

The results in Figure 4-5 imply that the pH of the solution may be an important factor, besides the sulfide concentration, for the appearance of signs that can be interpreted as SCC. The formation of Cu_2S which is believed to be the dominating corrosion reaction, produces hydroxide ions (Reaction 4-1). As outlined in Section 4.4, the driving force for corrosion increases greatly with decreasing pH. In terms of potential, a decrease in the pH by one unit can be translated to an increase in the driving potential for corrosion by about 30 mV, at 25 °C, all other terms assumed constant. (A decrease by one pH unit increases the potential along the hydrogen line by about 59 mV and the slope of the equilibrium line for $Cu(s)/Cu_2S(s)$ is about 59/2 mV per pH unit.) The increase in driving potential increases to more than 30 mV per pH-unit, with increasing temperature.

Higher driving voltage for a corrosion reaction allows higher spatial separation between anode and cathode. More non-uniform corrosion, for example in the form of intergranular corrosion, is thereby expected at lower pH than at higher pH. At least, the possibility for more non-uniform corrosion increases with decreasing pH. More non-uniform corrosion is also favored by the higher solubility of Cu_2S at lower pH.

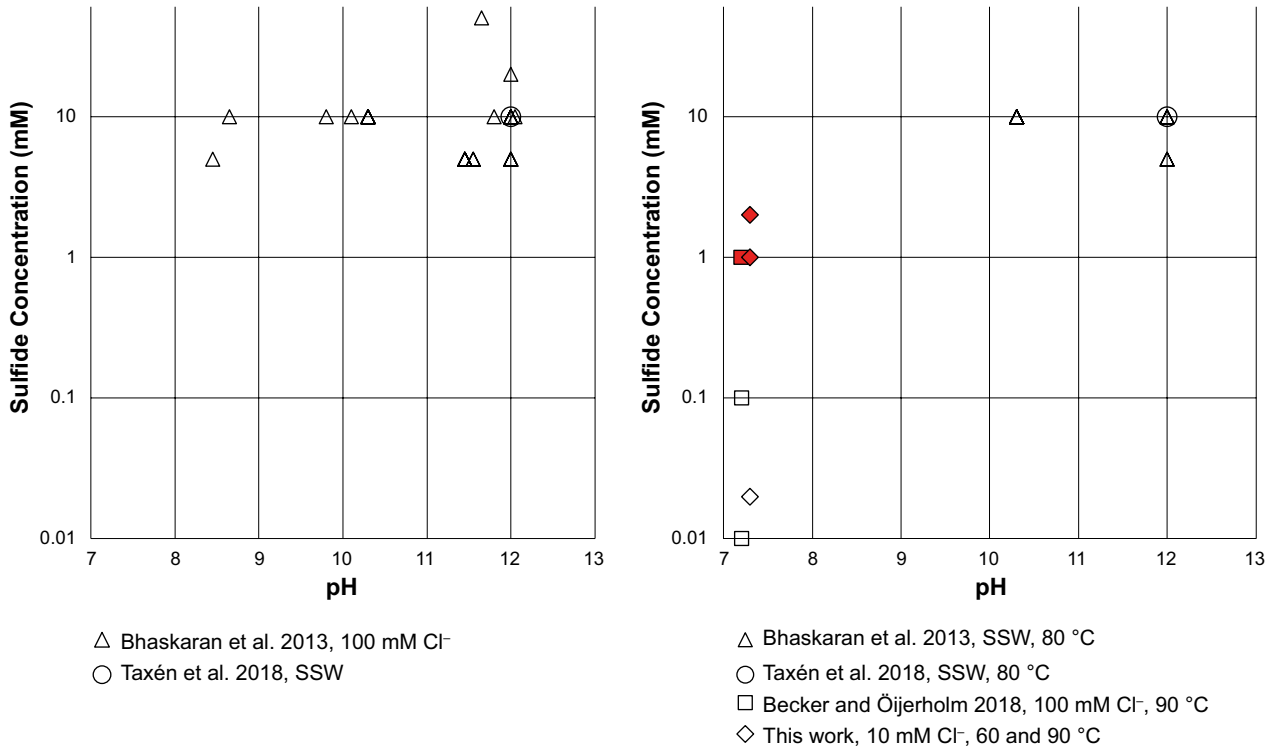

Figure 4-5. *Summary of the experimental result from previous work on SSRT testing of SKB-copper. Room temperature results in the left diagram and results for higher temperatures in the right diagram. Red symbols indicate conditions where signs of SCC were found.*

4.13 Intergranular corrosion and previous work

The crack-like features found by Becker and Öijerholm (2017) seem to be intergranular. Cracks run in all directions so that the direction of the strain can only be guessed in the images showing the outer surface. Intergranular corrosion or possibly initial defects are found in images from their experiments at 0.1 mM sulfide as well their experiments at 1.0 mM sulfide.

Taniguchi and Kawasaki (2008) make the distinctions of finding IGC at 1 mM sulfide, concave pitting at 5 mM sulfide and intergranular SCC at 10 mM sulfide. For 1 mM sulfide they show an intergranular, crack-like feature at approximately 45° angle to the surface. For 5 mM sulfide they show a crack-like feature with rounded profile and for 10 mM sulfide they present an approximately 50 µm deep intercrystalline, crack-like feature at about 90° angle to the surface. At first glance it appears that very little corrosion has occurred, at 10 mM sulfide, since the two flanks of the crack have profiles that seem to fit perfectly. On closer examination of their Figure 11, the flanks do not fit at all. There is a considerable mismatch, almost as if an oddly shaped grain is missing, alternatively there has been considerable corrosion of at least one grain boundary. Final attribution of SCC to the test in 10 mM sulfide is made by the decrease in strain at final rupture (Taniguchi and Kawasaki 2008).

In summary, intergranular corrosion was found by both Taniguchi and Kawasaki (2008) and Becker and Öijerholm (2017). In no experiment has the attack progressed to more than one grain from the surface. It remains an open question whether intergranular corrosion has transitioned into a different mechanism of SCC in any of the studies quoted.

4.14 Proposed mechanism

Figure 4-4 is useful as background illustration of localized corrosion. But, the crack-like features found in the present work do not look like that.

At point *C* the SEM-images show extremely thin or non-existing films or films that are very fragmented located at some distance from the metal. The surfaces at point *C* seems relatively unprotected against corrosion. No direct barrier against sulfide diffusing to the surface is seen.

At point *B* the SEM-images also show no protective layer. The metal surfaces seem free from solid corrosion products. Instead solid particles are found in the middle of the channel where they barely touch the flanks. Point *A* shows no solid corrosion products.

The difference in film behavior between the present study and the findings of Chen et al. (2014) may be explained by stress and strain. They generally found adherent although sometimes porous and poorly protecting films. In the present experiments the solid corrosion products are generally detached from the surface. Radial contraction of the test rod may be an important factor for film detachment and rupture.

This difference between film behavior with and without stress could qualify the observation as a case of SCC according to film rupture mechanism but the film rupture is not local and generally does not increase the mass transport rate of sulfide at any specific site. The impression is that mass transport of sulfide is not a limiting factor in the present study. This impression is based on the existence of grains of corrosion product, with the same appearance as copper sulfide, deep into the cavities (e.g. Figure 3-5, left column of images and Figure 3-8) and signs of corrosion without nearby solid corrosion products (e.g. Figure 3-10). The observation of corrosion without solid corrosion products implies that the corrosion products were dissolved. Having excluded chloride as a complex former in 1 mM sulfide (Section 4.4), aqueous sulfide complexes are the most probable form of the corrosion product. Large parts of the metal seem uncovered (at the scale of the SEM-images) and are probably corroding but at rates that are not limited by the diffusion of sulfide.

The mechanism of the intergranular corrosion seems to produce dissolved copper species rather than the solid. Cu_2S generally precipitates as secondary corrosion product at some distance from the metal surface. Similar results were found by Chen et al. (2018) but with no obvious intercrystalline corrosion. Where precipitation takes place outside a local corrosion attack, there is no net consumption of sulfide in the cavity. As indicated in Section 4.4, only a minute fraction of the sulfide binds to copper ions in the aqueous complexes. Propagation is made possible by diffusion of the primary aqueous corrosion

product to a sink in the form of a growing particle of Cu_2S, frequently located outside the cavity or local cavity. The formation of the aqueous complexes is pH-neutral and does not involve any other ions (Reactions 4-3 and 4-4). There should be no pH-gradient within a cavity where no solid precipitates. The chemical environment in the cavity is not significantly different from that outside the cavity. Yet precipitation or film formation does not always occur in the cavity. The concentrations of the primary corrosion products are limited by the electrochemical potential but apparently not by the solubility of $Cu_2S(s)$. The anodic reaction forms supersaturated solutions in the cavity. The difference in concentration between the level produced by the anodic dissolution and the level given by solubility is the driving force for diffusion. There are numerous examples where there are grains of solid corrosion product inside the cavity. These can serve as local sinks for the dissolved corrosion products and provide much shorter diffusion paths. Where $Cu_2S(s)$ forms in the cavity, this cavity has a net consumption of sulfide from the bulk so that a diffusion gradient arises. The formation of $Cu_2S(s)$ from dissolved complexes also consumes hydroxide so that there is an acidifying effect which increases the solubility of Cu_2S (Reactions 4-5 and 4-6). The acidifying effect can be counteracted by locating a part of the cathodic reaction, which increases the pH (Reaction 4-7), to the cavity.

The main part of the cathodic reaction probably takes place outside the cavity. The corrosion reaction as a whole, with Cu_2S and H_2 as products (Reaction 4-1), produces also hydroxide ions and increases the pH. Higher pH in the cavity than outside is not consistent with the deduced supersaturation in the cavity.

4.15 Alternative mechanisms

Slip-dissolution and related models for SCC imply that the flanks of the cavity should be protected by solid corrosion products and that the layer of solids at the propagating front breaks under the strain and thereby allows propagation. We see few examples of cavities where the flanks or the propagating fronts are covered with solid corrosion products.

The film rupture mechanism can be said to be operative but as discussed in the previous section, the film ruptures almost everywhere and there is no localization of corrosion associated with sites of film rupture.

The propagation of a film fracture mechanism involves the cracking of brittle layer at the propagating front of a crack. We see no layer of any kind at the front of the local attacks.

Vacancy injection, as described by Huotilainen et al. (2018), involves the breaking of a protective film at the propagating front of a crack. The mechanism is actually considered to be a refinement of the common slip-oxidation mechanism of SCC, and not a separate new SCC mechanism per se (Huotilainen et al. 2018). The vacancy injection mechanism was specifically proposed for trans granular SCC (Aaltonen et al. 1996, 2003). We see only intergranular attacks.

Hydrogen embrittlement at the front of a propagating crack does not seem probable. The hydrogen evolving cathodic reaction is most likely preferentially located outside the cavities in the present study. A location within a cavity would produce a high local pH and build up a concentration of dissolved H_2 (Reaction 4-7). Both factors would make hydrogen evolution energetically unfavorable in a confined volume relative to an open surface. The only case where we find that hydrogen evolution inside a cavity would be energetically favorable is when precipitation of $Cu_2S(s)$ inside a cavity causes the local pH to decrease. Since only a small fraction of the oxidized copper forms $Cu_2S(s)$ in the cavity, only a small fraction of the cathode reaction is required to neutralize the pH.

Houtilanien et al. (2018) suggest yet another mechanism for the appearance of crack like features. “The preexisting manufacturing defects (which Becker and Öijerholm showed to exist also in the unexposed material, that had never been in contact with the sulfide containing environment) extending to the specimen surface, open up due to the effect of surface active sulfide species on the cohesive forces of the opposing surfaces of a defect.” Since the material tested in the present study is essentially the same as that tested by Becker and Öijerholm (2017), similar defects were most likely present also in the present study. Figure 3-21 shows a collection of three images with material imperfections from the cross section of the unexposed test rod.

There were also some imperfections in the manufacturing of the test rods, in the present study. These imperfections were grooves with similar width as depth and were preferentially located towards the ends of the gauge section.

In summary, the most probable of the alternative causes for the crack-like features found is that they are influenced by manufacturing defects that somehow interact with sulfide from the solution, at least under strain. There may not be a clear cut difference between a microscopic manufacturing defect and a grain boundary susceptible to IGC.

4.16 Deficiency and incompleteness in the proposed mechanism

One apparent deficiency in the proposed mechanism of IGC is that it seems to require relatively large differences in nobility between grain boundary and grain body. The flanks (grain body) do apparently not corrode while the front (grain boundary) does. Propagation is described as diffusion of dissolved copper from the front, past the flanks and to the outer surface where growing particles of Cu_2S serve as sinks for the dissolved copper. All surfaces are exposed to approximately the same sulfide concentration. The apparent inertness at the flanks could be explained if the material there was very noble so that the dissolved copper concentration conveyed a degree of immunity against corrosion. The less noble grain boundary at the propagating front produces a relatively high concentration of dissolved copper. Propagation requires diffusion and diffusion requires a concentration gradient. At some point at the flanks the concentration will be significantly lower than that produced at the propagating front. Yet, the material at the flanks appears as if immune. The required difference in nobility between the grain boundary and grain body can be estimated from Nernst's law. The steeper the concentration gradient within the cavity the higher the difference in nobility must be. Otherwise the flank will no longer be immune, but start to corrode. It was found that the cavity probably behaves as a net anode which means that current is carried by the ions in the solution. This electrolytic current is associated with an ohmic drop in potential. This drop in potential should be added to the value estimated from Nernst's law in order to estimate the required difference in nobility between grain boundary and grain body. Rather detailed calculations would have to be made in order to judge the validity of the proposed mechanism.

One possible explanation for the deduced necessary difference in apparent nobility would be if the material at the propagating front would be made particularly un-noble by stress and strain. Strain at the propagating front would then create new exposed copper surface that may behave as un-noble. Stress could presumably increase the free energy of copper atoms at the front of a crack also causing an un-noble behavior. The surface mobility model of SCC seems to imply a similar process, where copper atoms at a strained site move sideways to the crack wall, possibly assisted by sulfide ions.

The evidence for example from Figure 3-8 seems irrefutable. The influence of stress or strain in the corrosion of the deeper parts of the cavities would seem to be very small. Most of the corroded copper has diffused out from the cavity and the flanks at the mouth seem unprotected by any passivating film. However, an interaction with an existing flaw in the material cannot be excluded. Such flaws, both internal and at the surface was found in the unexposed test rod, Figure 3-21.

IGC is definitely observed in the present study and the deepest intergranular attacks seem to be adequately explained without referring to other mechanisms of SCC, with the exception of superficial film rupture. If other mechanisms have been operative, the effects are over shadowed by IGC.

4.17 Summary of the proposed mechanism

The first step in the process is that the surface film of copper sulfide breaks under the strain. The radial contraction of the test rod is probably a strong contributing factor to the loss of adherence and breaking of the initial surface film.

Corrosion initiates at susceptible grain boundaries and produces small cavities. The intergranular corrosion is aggravated by strain that pulls apart the grains that form the flanks of the cavity. A wedge shaped cavity results. The corrosion produces mainly dissolved copper sulfide complex species. The local solution produced by corrosion at the grain boundary becomes supersaturated with respect to

solid copper sulfide, Cu_2S. Precipitation of Cu_2S takes place mostly outside the cavity although some Cu_2S is formed also in the cavity. The net consumption of sulfide in the cavity is relatively small and the supply of sulfide to the propagating front does not seem to limit the propagation rate. The rate of propagation is instead limited by the diffusion of the dissolved copper sulfide complex species. The sink for the dissolved copper is growing particles of $Cu_2S(s)$ that maintains the concentration gradient from supersaturation at the front of the cavity towards near equilibrium outside the cavity. Eventually, grains of Cu_2S begin to grow also inside the cavity. These grains provide shorter diffusion paths from sites of propagation (high concentration) to the sink (low concentration).

No adhering films of Cu_2S are formed in the cavity, at least at a thickness visible in SEM. The grains that form the walls of the cavity are probably corroding, but only slowly. The low corrosion rate at the walls of the cavity can be explained in part because corrosion at the grain boundary has left a near perfect crystal surface, in part also because of near electrochemical equilibrium between the perfect crystals and the copper containing solution.

4.18 Projected development of intergranular corrosion

The cavities created by IGC under straining conditions in 1 mM sulfide solution were formed during a period of about 14 days which poses a strong limit about making projections for future development.

A tendency for a shift in the mechanism can be discerned. The cavities seem to have grown by diffusion of dissolved copper sulfide complex species out from the cavity. Growing crystals of Cu_2S inside the cavity can be seen as a change in mechanism of propagation. In the first phase, the cavity does not consume sulfide. All sulfide that goes into the cavity comes out again as copper sulfide complex species, although only a very small fraction of the sulfide is bound to copper. There are no solids that limit the aqueous cross section in the cavity but a relatively long diffusion path to the sink in the form of growing particles of Cu_2S outside the cavity. In the second phase this diffusion path becomes much shorter as such sinks form inside the cavity. The part of the cavity that is located between the propagating front and the grains of Cu_2S inside the cavity behave in the same way as during the first phase. There is no net consumption of sulfide there. But the cavity as whole now consumes sulfide. Sulfide diffuses from the bulk to the site where solid Cu_2S forms, in order to maintain the sulfide concentration in the cavity. The Cu_2S grains occupy a part of the cross section available for diffusion of sulfide to the inner part of the cavity. Eventually the inner part of the cavity becomes depleted of sulfide as Cu_2S crystals continue to grow and the supply of sulfide becomes restricted by the size of the Cu_2S grains.

Worst case would seem to be when no or very little solid Cu_2S forms in the cavity. The diffusion path increases but such a cavity could continue to grow at an ever lower rate. This case is deemed highly unlikely. Grains of Cu_2S are seen in practically all cavities after 14 days. Deeper cavities with more and larger Cu_2S grains in the cavity imply that there will be more sites available for crystal growth, and very little dissolved copper will reach the mouth of the cavity. Chen et al. (2018) found that all available sulfide ended up as $Cu_2S(s)$, in their experiment. Without available sulfide there would be no corrosion and no dissolved copper. It is concluded that all oxidised copper ends up as $Cu_2S(s)$, as well as all available sulfide. Because of the volume increase when copper metal is corroded to Cu_2S, the cavity will tend to fill up with Cu_2S. Finally, the cavity will be unable to grow further. Such a cavity may be reactivated if there is a strain that creates a new aqueous path between the mouth of the cavity and the copper metal.

5 Conclusions

Copper was tested by slow straining at a rate of 5×10^{-7} s^{-1} in solutions of NaCl with additions of various levels of sulfide. The test solution was buffered to about pH 7.2 by 10 mM phosphate. Cross sections of the surfaces were studied with SEM, and the observations could be summarized:

- Intergranular corrosion in the shape of cracks was observed at a level of 1 mM sulfide at 60 °C and at 90 °C.
- Tests under identical conditions with 0.02 mM sulfide did not result in such intergranular corrosion but only an uneven, blackened corroded surface.
- Stress-strain curves do not reveal any signs of stress corrosion cracking. The time to final fraction and the elongation at rupture are independent of the test conditions used.
- Intergranular corrosion in the shape of cracks develops early during the test. Tests interrupted after 2 or 4 days of straining reveal a number of cracks preferentially located towards the ends of the gauge length of the test rod.
- At final rupture of the test rods, after about 14 days of continuous strain, the cracks are more evenly distributed along the test rod.
- Necking and final rupture occurs close to the middle of the gauge length and not at the location where the first cracks appear.
- The maximum depth of the cracks is estimated to about 20–30 µm after final rupture. Cracks after 2 or 4 days testing were estimated to be about 10–20 µm deep. Under similar testing conditions, in the test until rupture no crack deeper than about 20 µm was found.
- Protective layers of corrosion products are reported under similar conditions, when there is no strain. In the present study the innermost layer is cracked, presumably by the strain. Intergranular corrosion becomes possible at sites where gaps in the layer of corrosion product coincides with a grain boundary that is susceptible to intergranular corrosion.

A mechanism to explain the observed mode of corrosion and the observed shape and depths of the cavities formed is suggested. According to the mechanism suggested, the cavities are predicted to fill up with solid copper sulfide which will act as a barrier between aqueous sulfide and copper metal. Further propagation of such a cavity would be possible only if the cavity is widened by strain, creating a new path for sulfide. A cavity thus reactivated will again tend to fill up with solid copper sulfide.

References

SKB's (Svensk Kärnbränslehantering AB) publications can be found at www.skb.com/publications.

Aaltonen P, Saario T, Karjalainen-Roikonen P, Piippo J, Tähtinen S, Itäaho M, Hänninen H, 1996. Vacancy-creep model for EAC of metallic materials in high temperature water. In Proceedings of Corrosion 96, Denver, Colorado, 25–28 March 1996. NACE International, Paper 81.

Aaltonen P, Jagodzinski Y, Hänninen H, 2003. Vacancy generation in electrochemical oxidation/dissolution of copper in $NaNO_2$ solution and its role in SCC mechanism. In Moody N R, Thompson A W, Ricker R E, Was G W, Jones R H (eds). Hydrogen effects on material behavior and corrosion deformation interactions. Proceedings of the International Conference on Hydrogen Effects on Material Behavior and Corrosion Deformation Interactions, held at Jackson Lake Lodge, Wyoming, 22–26 September 2002. Pittsburgh, PA: TMS (The Minerals, Metals, and Materials Society), 597–606.

Aaltonen P, Yagodzinskyy Y, Saukkonen T, Kilpeläinen S, Tuomisto F, Hänninen H, 2015. Role of excessive vacancies in transgranular stress corrosion cracking of pure copper. Corrosion Reviews 33. doi:10.1515/corrrev-2015-0047

Aboubakr M A, Al-Kharafi F M, Ateya B G, 2006. Intergranular corrosion of copper in the presence of benzotriazole. Scripta Materialia 54, 1 673–1 677.

Al Kharafi F M, Ghayad I M, Ateya B G, 2008. Rapid intergranular corrosion of copper in sulfide-polluted salt water. Electrochemical and Solid-State Letters 114, G15–G18.

Bard A J, Faulkner L R, 1980. Electrochemical methods: fundamentals and applications. New York: Wiley.

Becker R, Öijerholm J, 2017. Slow strain rate testing of copper in sulfide rich chloride containing deoxygenated water at 90 °C. SSM report 2017:02, Swedish Radiation Safety Authority.

Bhaskaran G, Carcea A, Ulaganathan J, Wang S, Huang Y, Newman R C, 2013. Fundamental aspects of stress corrosion cracking of copper relevant to the Swedish deep geologic repository concept. SKB TR-12-06, Svensk Kärnbränslehantering AB.

Chen J, Qin Z, Shoesmith D W, 2014. Key parameters determining structure and properties of sulphide films formed on copper corroding in anoxic sulphide solutions. Corrosion Engineering, Science and Technology 49, 415–419.

Chen J, Qin Z, Martino T, Shoesmith D W, 2017. Non-uniform film growth and micro/macro-galvanic corrosion of copper in aqueous sulphide solutions containing chloride. Corrosion Science 114, 72–78.

Chen J, Qin Z, Martino T, Guo M, Shoesmith D W, 2018. Copper transport and sulphide sequestration during copper corrosion in anaerobic aqueous sulphide solutions. Corrosion Science 131, 245–251.

Dartmann J, Sadlowsky B, Dorsch T, Johannsen K, 2010. Copper corrosion in drinking water systems – effect of pH and phosphate-dosage. Materials and Corrosion 61, 189–198.

Fennell P A H, Graham A J, Smart N R, Sofield C J, 2001. Grain boundary corrosion of copper canister material. SKB TR-01-09, Svensk Kärnbränslehantering AB.

Gubner R, Andersson U, Linder M, Nazarov A, Taxén C, 2006. Grain boundary corrosion of copper canister weld material. SKB TR-06-01, Svensk Kärnbränslehantering AB.

Huotilainen C, Saario T, Toivonen A, 2018. Review of the Aaltonen-mechanism. SKB R-18-03, Svensk Kärnbränslehantering AB.

King F, Newman R, 2010. Stress corrosion cracking of copper canisters. SKB TR-10-04, Svensk Kärnbränslehantering AB.

King F, Lilja C, Pedersen K, Pikänen P, Vähänen M, 2010. An update of the state-of-the-art report on the corrosion of copper under expected conditions in a deep geologic repository. SKB TR-10-67, Svensk Kärnbränslehantering AB.

Mattsson E, 1980. Corrosion of copper and brass: practical experience in relation to basic data. British Corrosion Journal 15, 6–13.

Miyamoto H, Mimaki T, Vinogradov A, Hashimoto S, 2007. Intergranular corrosion of ultrafine grain copper fabricated by ECAP. Materials Science Forum 561–565, 2 385–2 388.

Mountain B W, Seward T M, 1999. The hydrosulphide/sulphide complexes of copper(I): Experimental determination of stoichiometry and stability at 22 °C and reassessment of high temperature data. Geochimica et Cosmochimica Acta 63, 11–29.

Mountain B W, Seward T M, 2003. Hydrosulfide/sulfide complexes of copper(I): Experimental confirmation of the stoichiometry and stability of $Cu(HS)2^-$ to elevated temperatures. Geochimica et Cosmochimica Acta 67, 3 005–3 014.

Newman R C, 2002. Stress-corrosion cracking mechanisms. In Marcus P (ed). Corrosion mechanisms in theory and practice. 2nd ed. New York: Marcel Dekker, 499–544.

Oudar J, 2002. Introduction to surface reactions: adsorption from gas phase. In Marcus P (ed). Corrosion mechanisms in theory and practice. 2nd ed. New York: Marcel Dekker, 19–51.

Puigdomenech I, Taxén C, 2000. Thermodynamic data for copper Implications for the corrosion of copper under repository conditions. SKB TR-00-13, Svensk Kärnbränslehantering AB.

Schock M R, Lytle D A, Clement J A, 1995. Effect of pH, DIC, orthophosphate and sulfate on drinking water cuprosolvency. EPA 600-R-95-085, National Risk Management Research Laboratory Office of Research and Development, US Environmental Protection Agency, Cincinnati, Ohio.

Smith J, Qin Z, King F, Werme L, Shoesmith D W, 2007. Sulfide film formation on copper under electrochemical and natural corrosion conditions. Corrosion 63, 135–144.

Smith J M, Qin Z, King F, Shoesmith D W, 2009. The influence of chloride on the corrosion of copper in aqueous sulphide solutions. In Proceedings of the SACNUC (Sulphur-Assisted Corrosion in Nuclear Waste Disposal Systems) Workshop, Brussels, 21–23 October 2008. European Federation of Corrosion.

Taniguchi N, Kawasaki M, 2008. Influence of sulfide concentration on the corrosion behavior of pure copper in synthetic seawater. Journal of Nuclear Materials 379, 154–161.

Taxén C, Wickström L, Sparr M, 2017. Corrosion properties of cold worked or welded copper materials. SKB R-17-09, Svensk Kärnbränslehantering AB.

Taxén C, Flyg J, Bergqvist H, 2018. Stress corrosion testing of copper in sulfide solutions. SKB TR-17-16, Svensk Kärnbränslehantering AB.

Yagodzinskyy Y, Malitckii E, Saukkonen T, Hänninen H, 2012. Hydrogen-enhanced creep and cracking of oxygen-free phosphorus-doped copper. Scripta Materialia 67, 931–934.

Arkitektkopia AB, Bromma, 2019

SKB is responsible for managing spent nuclear fuel and radioactive waste produced by the Swedish nuclear power plants such that man and the environment are protected in the near and distant future.

skb.se